iScience

CellPress
OPEN ACCESS

Article

Neural Circuit Mechanism Underlying the Feeding Controlled by Insula-Central Amygdala Pathway

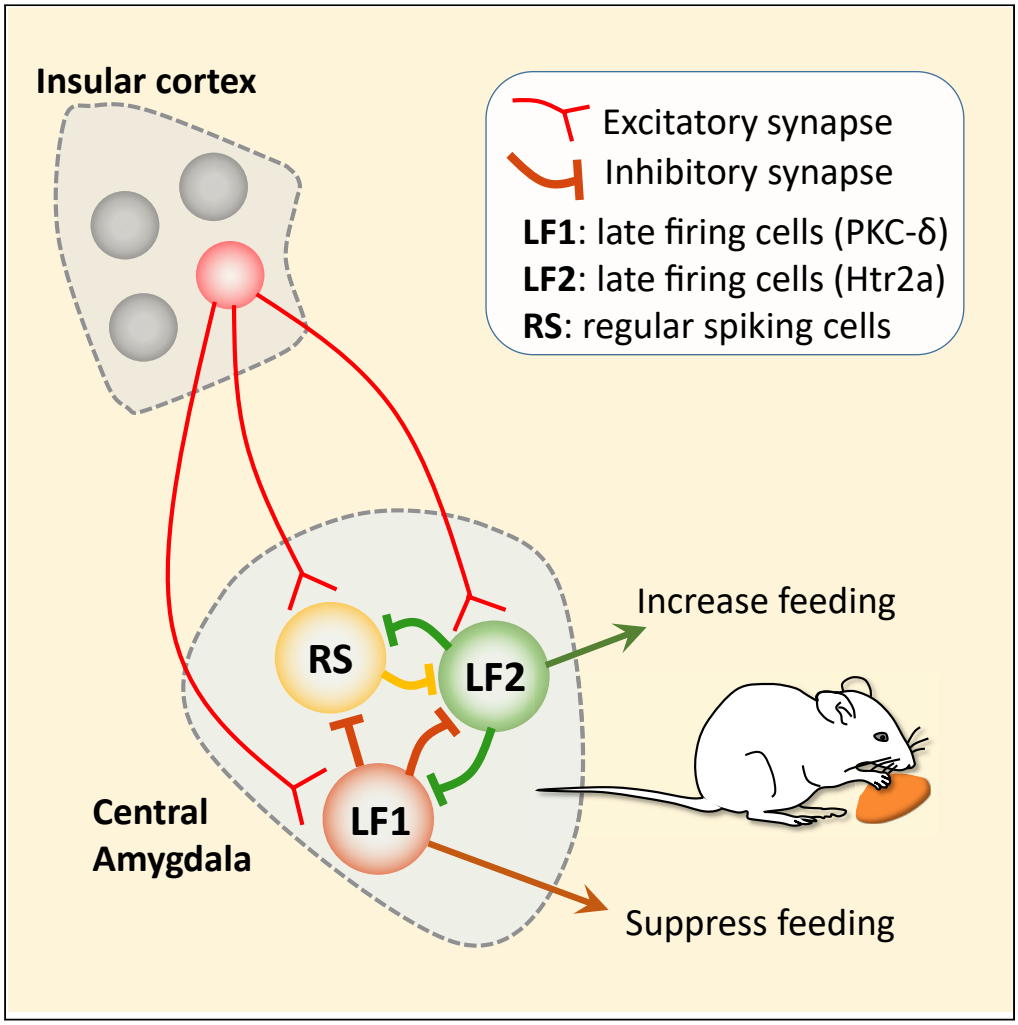

Calvin Zhang-Molina, Matthew B. Schmit, Haijiang Cai

calvinz@math.arizona.edu (C.Z.-M.)
haijiangcai@email.arizona.edu (H.C.)

HIGHLIGHTS

Activation of the insular cortex→central amygdala (CeA) pathway suppresses feeding

Insular cortex neurons send similar excitatory inputs to different types of CeA neurons

Model suggests a required circuit with both late firing and regular spiking cells

The circuit model can explain current and previous CeA-mediated feeding behaviors

Zhang-Molina et al., iScience *23*, 101033
April 24, 2020
https://doi.org/10.1016/j.isci.2020.101033

iScience

CellPress
OPEN ACCESS

Article

Neural Circuit Mechanism Underlying the Feeding Controlled by Insula-Central Amygdala Pathway

Calvin Zhang-Molina,[1,*] Matthew B. Schmit,[2,3] and Haijiang Cai[2,4,5,*]

SUMMARY

The Central nucleus of amygdala (CeA) contains distinct populations of neurons that play opposing roles in feeding. The circuit mechanism of how CeA neurons process information sent from their upstream inputs to regulate feeding is still unclear. Here we show that activation of the neural pathway projecting from insular cortex neurons to the CeA suppresses food intake. Surprisingly, we find that the inputs from insular cortex form excitatory connections with similar strength to all types of CeA neurons. To reconcile this puzzling result, and previous findings, we developed a conductance-based dynamical systems model for the CeA neuronal network. Computer simulations showed that both the intrinsic electrophysiological properties of individual CeA neurons and the overall synaptic organization of the CeA circuit play a functionally significant role in shaping CeA neural dynamics. We successfully identified a specific CeA circuit structure that reproduces the desired circuit output consistent with existing experimentally observed feeding behaviors.

INTRODUCTION

Neurons in the central nucleus of the amygdala (CeA) play an important role in controlling feeding, a behavior critical to our survival and health (Cai et al., 2014; Douglass et al., 2017; Hardaway et al., 2019; Ip et al., 2019; Petrovich et al., 2009). However, how the CeA neurons control food intake at circuit level is still poorly understood. The CeA is primarily composed of γ-aminobutyric acid (GABAergic) inhibitory neurons, which can be classified into multiple different types based on their gene expression profiles or distinct electrophysiological properties (Chieng et al., 2006; Ciocchi et al., 2010; Day et al., 1999; Fadok et al., 2018; Haubensak et al., 2010; Kim et al., 2017; Lopez de Armentia and Sah, 2004; McDonald and Augustine, 1993; Sah et al., 2003). Using genetic markers, several recent studies identified at least two distinct populations of neurons in the CeA that play opposing roles in controlling feeding (Cai et al., 2014; Douglass et al., 2017). Specifically, one study found that activation of the neurons marked by the expression of protein kinase C-delta (PKC-δ+) suppresses food intake, whereas silencing these neurons increases food intake in fed state (Cai et al., 2014). Another study identified a different population of neurons marked by the expression of the serotonin receptor 2a (Htr2a+), which do not overlap with PKC-δ+ neurons (Douglass et al., 2017). In contrast to PKC-δ+ neurons, activation of the Htr2a+ neurons increases food intake, whereas silencing these neurons suppresses food intake (Douglass et al., 2017). Particular physiological properties give rise to distinctive discharge patterns and might play important roles in controlling functions of the neurons during behaviors. Based on their action potential firing in response to injection of depolarization currents, neurons in the CeA are usually classified into three types: (1) late firing neurons and (2) regular spiking neurons, which are mostly observed in the lateral part of CeA, and (3) low threshold bursting neurons, which are usually in the medial part of CeA (Chieng et al., 2006; Dumont et al., 2002; Lopez de Armentia and Sah, 2004). Interestingly, both PKC-δ+ and Htr2a+ neurons are primarily located in the lateral part of CeA and contain mostly late firing neurons and a small proportion of regular spiking populations (Cai et al., 2014; Douglass et al., 2017). Thus, the distinct functions in feeding of these two populations of neurons cannot be explained by their electrophysiological properties. Another possibility for these neurons to have distinct functions is that they receive inputs from different upstream brain regions and are thereby activated in different situations to control feeding. One dominant top-down cortical input to the CeA and other amygdala subnuclei is from the insula (Fudge and Tucker, 2009; McDonald et al., 1999; Mufson et al., 1981; Shi and Cassell, 1998), which contains neurons that play important roles in processing taste and visceral information (Accolla and Carleton, 2008; Andermann and Lowell, 2017; Augustine, 1996; Caruana et al., 2011;

[1]Department of Mathematics, University of Arizona, Tucson, AZ 85721, USA

[2]Department of Neuroscience, University of Arizona, Tucson, AZ 85721, USA

[3]Graduate Interdisciplinary Program in Neuroscience, University of Arizona, Tucson, AZ 85721, USA

[4]Bio5 Institute and Department of Neurology, University of Arizona, Tucson, AZ 85721, USA

[5]Lead Contact

*Correspondence: calvinz@math.arizona.edu (C.Z.-M.), haijiangcai@email.arizona.edu (H.C.)

https://doi.org/10.1016/j.isci.2020.101033

Chen et al., 2011; Craig, 2003; Gogolla, 2017; Katz et al., 2001; Samuelsen and Fontanini, 2017; Yamamoto et al., 1985). Recent studies reported that the projection from insular cortex to CeA signals aversive bitter taste as tested in drinking behaviors (Schiff et al., 2018; Wang et al., 2018), suggesting this pathway might also control feeding behavior. However, whether the insula-CeA pathway regulates solid food intake and what type of CeA neurons are innervated by the inputs from insular cortex are still unknown.

Here we find that optogenetic activation of the insula-CeA pathway strongly and rapidly suppresses feeding. Surprisingly, our optogenetics-assisted circuits mapping show that insular cortex neurons send monosynaptic excitatory inputs non-selectively to all CeA neurons with similar strength, independent of their genetic markers or electrophysiological properties. Based on these results and previously published data on CeA neurons, we developed a conductance-based dynamical systems model for the CeA circuit to explore the possible underlying circuit structure of CeA neurons in feeding control. Interestingly, of the ten fundamentally different circuit structures considered, only one specific circuit structure was able to consistently generate the observed feeding behaviors. Computer simulations of our CeA circuit model revealed that both the regular spiking and the late firing CeA neurons play an essential role in modulating the CeA circuit function and only one specific combination of the individual CeA neurons' electrophysiological properties and the CeA circuit's synaptic organization can reproduce the desired circuit output.

RESULTS

Activation of the Projection from Insular Cortex to CeA Suppresses Feeding

In order to specifically target the insular cortex neurons that project to the CeA, we used a two-virus Cre-on strategy, in which we stereotaxically injected Cre-dependent adeno-associated virus (AAV) encoding channelrhodopsin (ChR2) (Zhang et al., 2007) or enhanced yellow fluorescent protein (EYFP) control into the insular cortex and AAVretro-Cre (Tervo et al., 2016) into the CeA bilaterally in wild-type mice. Meanwhile, we implanted optic fibers above the CeA. Thus, only the nerve terminals in CeA that projected from insular cortex neurons express ChR2 and can be activated by light stimulation (Figure 1A). Histological analysis revealed that ChR2-expressing neurons were restricted to a sub-region of the insular cortex (Figures 1B and 1C). Interestingly, the fluorescent nerve terminals projected from these insular cortex neurons were remarkably exclusive to the lateral part of CeA but not to the surrounding regions (Figure 1D). Three to four weeks after virus expression and animal recovery, we coupled the optic fibers to a blue laser (473 nm) to stimulate the CeA terminals projected from insular cortex neurons. We found that photo-stimulation of these terminals reduced the total amount of food intake in both fed (Figure 1E) and 24-h-fasted animals (Figure 1F). Light activation of this pathway also significantly increased the latency to eat (Figure S1), suggesting the initiation of feeding is also inhibited. Light stimulation of the insula-CeA neural pathway does not affect the movement or anxiety levels significantly as tested in an open field assay (Figures 1I–1L). We also tested feeding when the mice were in their home cages, where the mice were less anxious. Mice were 24-h fasted and either blue light or control light (593 nm), which does not activate ChR2, was delivered 1–2 s after the onset of eating. We found that light stimulation of the insula-CeA pathway significantly shortened the duration of feeding bouts (Figures 1G and 1H), indicating that feeding was suppressed in the home cage. These results suggest that insular cortex stimulation is able to reduce total food intake as well as bout duration and that this is not a result of anxiety or of any impaired mobility.

CeA Neurons Receive Monosynaptic Excitatory Inputs from Insular Cortex

To determine if CeA neurons are monosynaptically innervated by inputs from insular cortex neurons, we stereotaxically injected AAV encoding ChR2-EYFP in insular cortex in wild-type mice. After allowing 3–4 weeks for post-surgical recovery and virus expression, we prepared live brain slices and performed whole-cell patch clamp recording on neurons in the CeA (Figures 2A–2C). The brain sections that contained insular cortex were also cut to verify the ChR2-EYFP expression in insular cortex neurons. We found that the EYFP-positive nerve fibers were restricted to the CeA region (Figure 2B). Although the soma of the neural projections from insular cortex were cut away in the brain slices with the CeA, we found that optogenetic activation of the ChR2-expressing terminals in CeA is sufficient to trigger postsynaptic responses in CeA neurons. When the cells are voltage clamped at −70 mV, we observed robust light-triggered excitatory postsynaptic currents (EPSCs), which can be blocked by the competitive AMPA/kainate receptor antagonist CNQX (Figure 2D). All these EPSCs are triggered within a short delay of less than 4 ms after the light pulses (Figure 2D inset), suggesting the connection is monosynaptic. Almost all the CeA neurons tested (32 of 33 tested cells) show EPSCs in response to light pulses. This result is consistent with a previous study that reported nearly all CeA neurons receive excitatory innervation from insular cortex (Schiff et al., 2018) and also consistent with the previous monosynaptic retrograde rabies tracing studies, which demonstrated

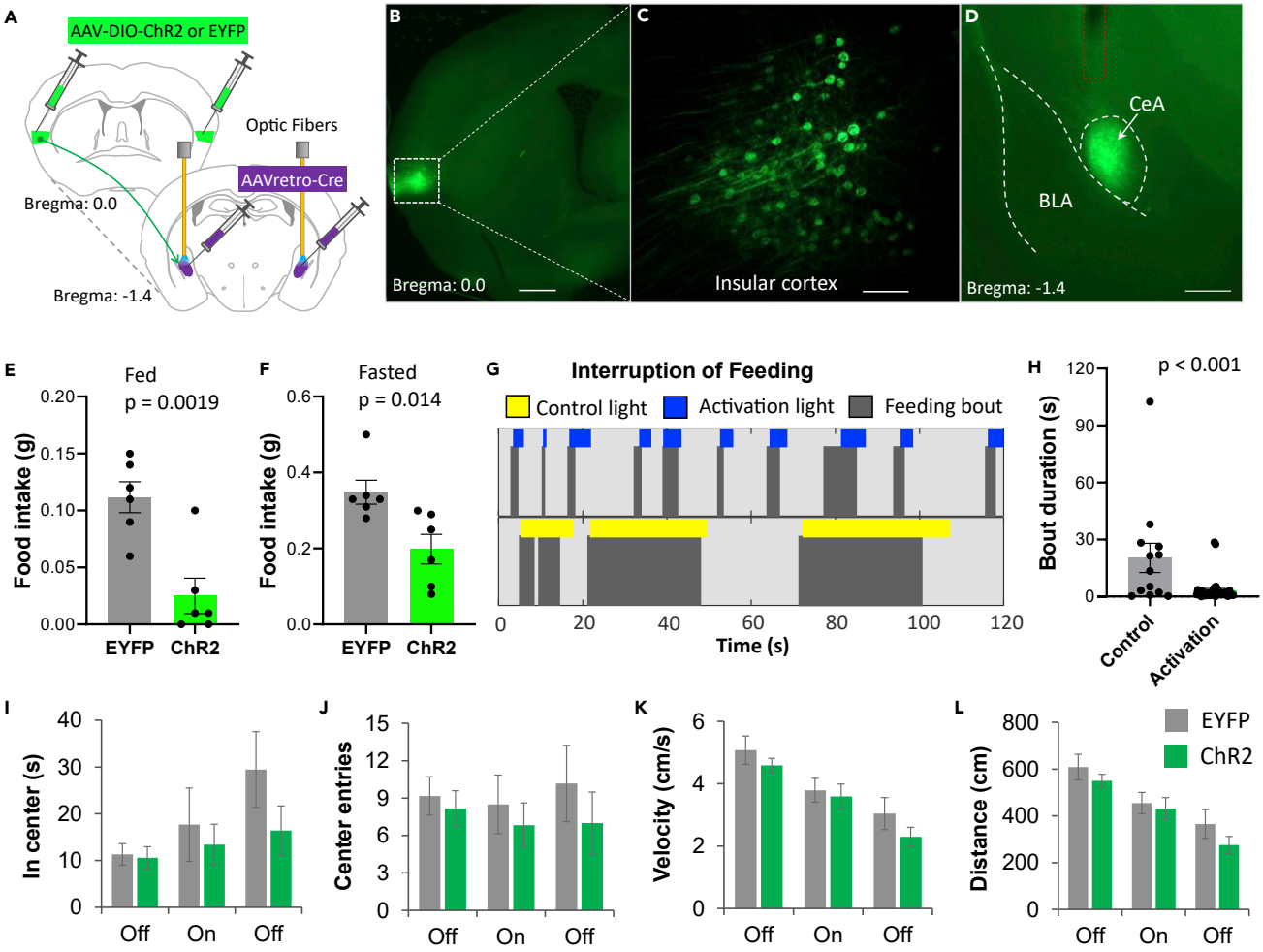

Figure 1. Optogenetic Activation of the Insula-CeA Projection Suppresses Food Intake

(A) Diagram shows virus injection strategy and optic fiber implantation.

(B) ChR2-EYFP expression in insular cortex neurons verified in histology post experiments. Scale bar, 500 μm.

(C) High-resolution image shows EYFP expression in individual insular cortex neurons. Scale bar, 100 μm.

(D) EYFP fluorescent nerve terminals are restricted in CeA region. Red dotted line outlines the optic fiber tract. Scale bar, 500 μm.

(E) Food intake in fed mice after light stimulation of the insula-CeA projections in a feeding session of 30 min. Light pulse 10 ms, 10 Hz. Unpaired t test, $t_{(10)}$ = 4.19. n = 6 animals in each group.

(F) Food intake in 24-h-fasted mice after light stimulation of the insula-CeA projections in a feeding session of 20 min. Light pulse 10 ms, 10 Hz. Unpaired t test, $t_{(10)}$ = 2.99. n = 6 animals in each group.

(G) A representative raster plot shows that feeding bouts are interrupted by light stimulation. Light pulses were usually delivered 1–2 s after the feeding was started. Mice were 24 h fasted and tested in their home cages.

(H) Quantification of the feeding bout duration after light stimulation. Unpaired t test, $t_{(48)}$ = 3.56. n = 13 bouts in control and 37 bouts in activation group.

(I–L) Light stimulation does not impair movement or anxiety in the open field test. Light pulses (10 ms, 10 Hz, 2 min) were delivered after 2 min no light base line and followed by 2 min post light.

Two-way ANOVA. No difference between EYFP and ChR2 was detected. n = 6 animals in each group. Data shown as mean ± SEM.

that both CeA PKC-δ+ neurons and CeA Htr2a+ neurons receive monosynaptic inputs from neurons in insular cortex (Cai et al., 2014; Douglass et al., 2017). Interestingly, when we voltage clamped CeA neurons at −40 mV, we observed robust upward inhibitory postsynaptic currents (IPSCs) following the downward EPSCs, both of which are blocked by CNQX (Figure 2E). Given the fact that all CeA neurons are GABAergic inhibitory neurons (Haubensak et al., 2010; Sun and Cassell, 1993) and the mutual inhibition between CeA neurons described in previous studies (Hou et al., 2016; Hunt et al., 2017), these results suggest that the IPSCs are disynaptic to the insular cortex inputs and are the result of GABAergic inhibition from other CeA neurons activated by light-stimulated insular cortex inputs (Figure 2F).

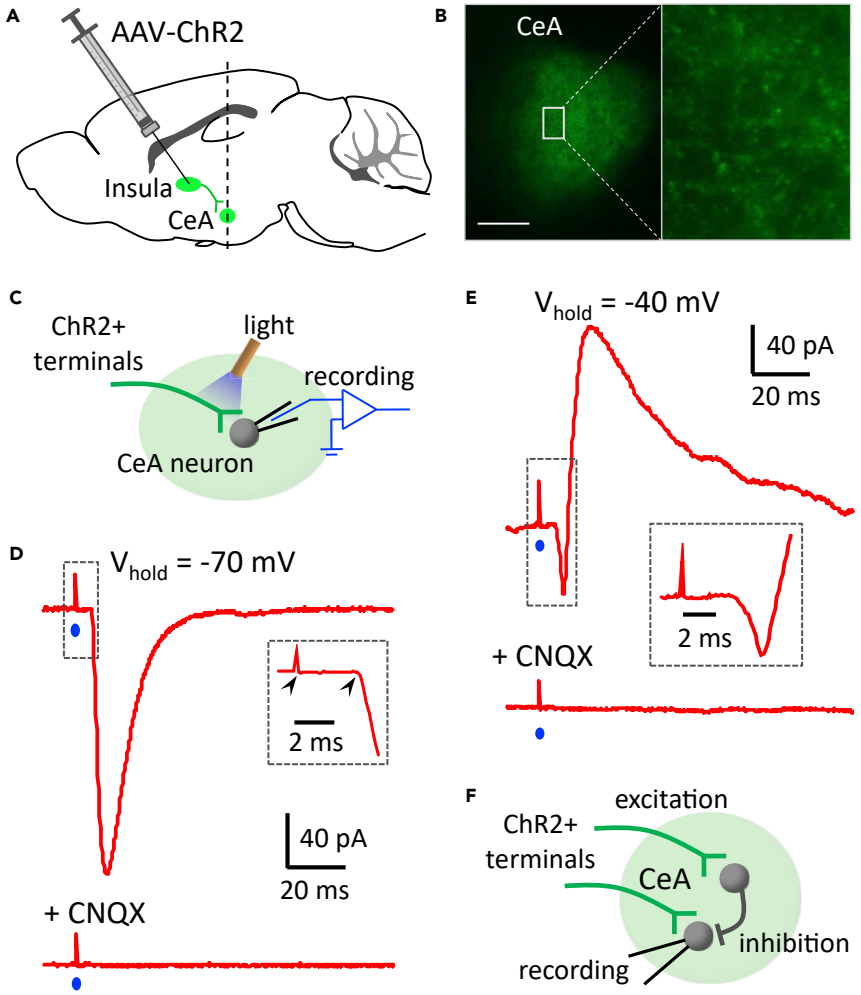

Figure 2. CeA Neurons Receive Monosynaptic Excitatory Inputs from Insular Cortex

(A) Diagram shows virus injection and brain slices with CeA were cut for electrophysiological recording.

(B) A representative image shows that the fluorescent nerve terminals are located in CeA of live brain slices. Scale bar, 200 μm.

(C) Diagram shows light stimulation of the ChR2-expressing nerve terminals and electrophysiological recording on CeA neurons.

(D) Sample recording traces show that light pulse (blue dot) triggers EPSC in a CeA neuron when it is voltage clamped at −70 mV and this EPSC is blocked by bath application of 20 μM CNQX. Inset, the latency of the EPSC is measured from the start of light to the start of inward current (arrows).

(E) Sample recording traces show that light pulse triggers both EPSC and IPSC in a CeA neuron when it is voltage clamped at −40 mV. Both the EPSC and IPSC are blocked by CNQX (20 μM).

(F) The circuit connection suggested by the electrophysiological recording results.

Insular Cortex Neurons Innervate CeA Neurons Non-selectively

Because activation of the insular-CeA pathway suppresses food intake, the same effect seen with the activation of CeA PKC-δ+ neurons, we hypothesize that the excitation from insular cortex to CeA PKC-δ+ neurons (PKC-δ+) is stronger than that in PKC-δ negative (PKC-δ-) neurons. In order to identify the PKC-δ+ neurons during slice recording, we crossed the PKC-δ-Cre mice with the AI14 Cre-reporter line (Madisen et al., 2010) to express tdTomato in PKC-δ+ neurons. Our previous study has shown that almost all the CeA PKC-δ+ neurons (>99%) are labeled by tdTomato in this way (Cai et al., 2014). With this strategy, we can identify CeA PKC-δ+ neurons by their tdTomato expression in live brain slices (Figure 3A). We stereotaxically injected an AAV encoding ChR2-EYFP in the insular cortex of the PKC-δ-Cre-AI14 crossed mice. Three to four weeks after virus injection, we performed slice electrophysiological recording on CeA neurons. We first current clamped the neurons and applied a series of depolarization steps to elicit action potential firing,

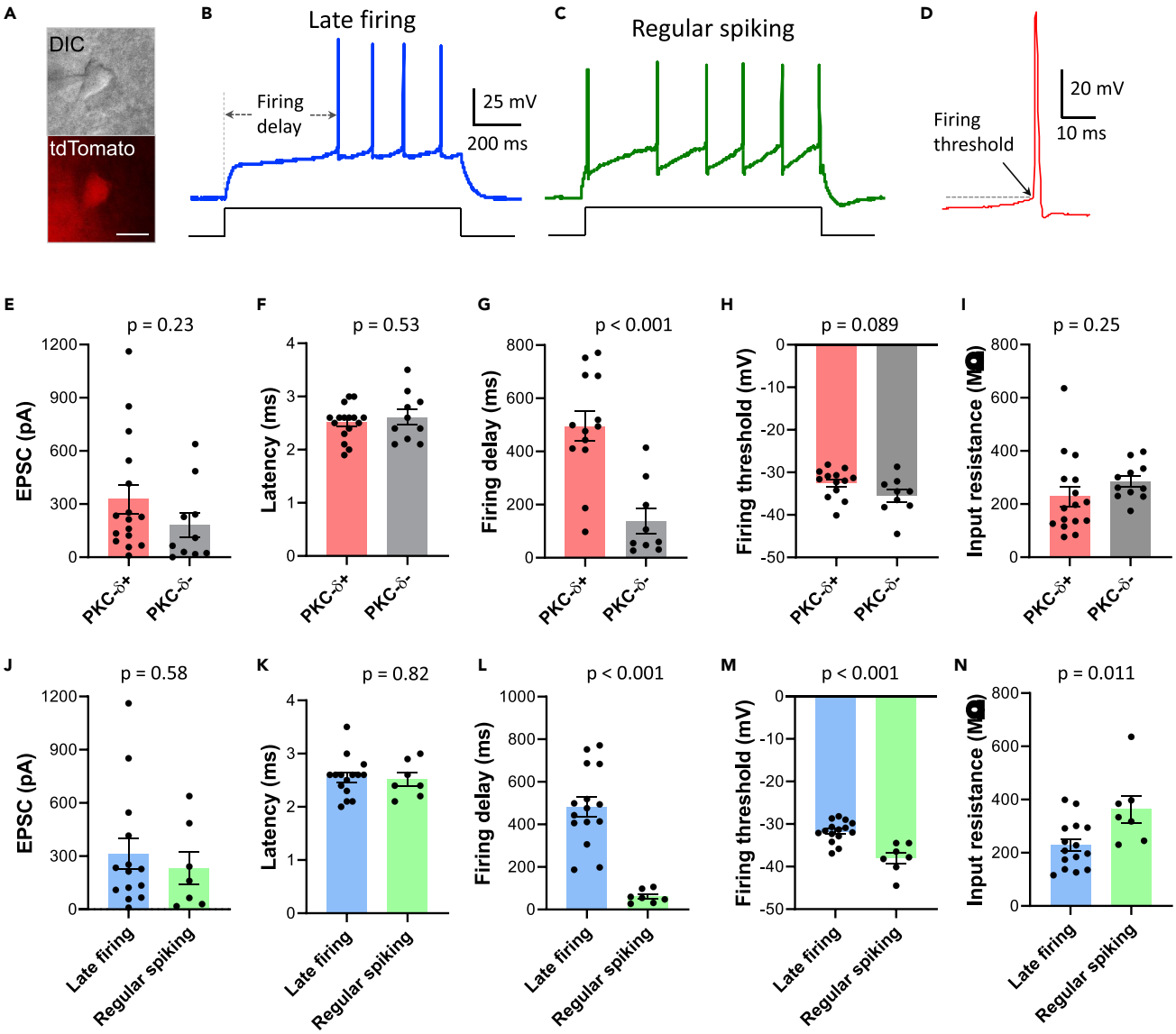

Figure 3. Insular Cortex Innervates CeA Neurons Nonselectively

(A) PKC-δ+ neurons can be identified by tdTomato expression in brain slices. DIC, differential interference contrast. Scale bar, 10 μm.

(B) Sample recording trace of a late firing neuron in response to a step of depolarizing current injection.

(C) Sample recording trace of a regular spiking neuron in response to a step of depolarizing current injection.

(D) Firing threshold identified in a sample recording trace of an action potential.

(E–I) EPSC (E), EPSC latency (F), action potential firing delay (G), action potential firing threshold (H), and input resistance (I) in PKC-δ+ neurons and PKC-δ- neurons. Unpaired t test. $t_{(24)} = 1.23$ (E), $t_{(24)} = 0.64$ (F), $t_{(20)} = 4.59$ (G), $t_{(20)} = 1.79$ (H), $t_{(25)} = 1.18$ (I). n = 13–16 PKC-δ+ neurons and 9–11 PKC-δ- neurons.

(J–N) EPSC (J), EPSC latency (K), action potential firing delay (L), action potential firing threshold (M), and input resistance (N) in late firing neurons and regular spiking neurons.

Unpaired t test, $t_{(19)} = 0.57$ (J), $t_{(20)} = 0.23$ (K), $t_{(20)} = 6.07$ (L), $t_{(20)} = 4.84$ (M), $t_{(20)} = 2.80$ (N). n = 14–15 late firing neurons and 7 regular-spiking neurons. Data shown as mean ± SEM.

which were used to characterize electrophysiological properties of the recorded neurons (Figures 3B–3D). We then voltage clamped the neurons and elicited EPSCs by photo-stimulating the nerve terminals projected from insular cortex. Although there is a trend toward larger EPSCs in PKC-δ+ neurons than in PKC-δ- neurons, we did not observe a significant difference (Figure 3E). The EPSC latency in both populations was around 3 ms (Figure 3F), suggesting monosynaptic innervation. We also checked the electrophysiological properties of these neurons (Figures 3G–3I). Our only observed difference was a significantly

longer delay in action potential firing in response to the injection of a depolarizing current (Figures 3B and 3G), which is consistent with a previous report that shows majority of the PKC-δ+ neurons are late firing neurons (Haubensak et al., 2010).

Neurons in the CeA are usually classified into three different types based on their responses to depolarization current injections (Chieng et al., 2006; Dumont et al., 2002; Lopez de Armentia and Sah, 2004). The neurons that show a significant delay before firing action potentials are classified as late firing neurons (Figure 3B), whereas neurons that fire without this delay are classified as regular spiking neurons (Figure 3C). A third type of neurons that do not display such delay but show bursting activity and sometimes a rebound firing post hyperpolarization are classified as low threshold bursting neurons. Confirming previous findings, we found that late firing neurons and regular spiking neurons are mostly located in the lateral part of CeA, whereas low threshold bursting neurons are usually observed in the medial part of CeA. Because both the PKC-δ+ neurons and Htr2a+ neurons are located in the lateral part of CeA, we focus on the late firing neurons and regular spiking neurons. Comparing EPSC properties between these two populations, we did not observe any significant difference in EPSC amplitude or latency (Figures 3J and 3K). Consistent with previous reports, the electrophysiological properties of these two types of neurons are significantly different (Figures 3L–3N). Together, these results suggest that the projection from the insular cortex to CeA neurons is non-selective and, at the overall population level, insular neurons innervate all types of CeA neurons with similar strength despite their distinct genetic markers or electrophysiological properties.

Activation of Insula-CeA Projections Trigger Action Potential Firing in CeA Neurons

We next tested whether stimulating the insula-CeA projections differentially activates distinct populations of CeA neurons. When we current clamped the CeA neurons and light activated the ChR2-expressing terminals projected from insular cortex, we found that, in many cases, a brief light pulse can trigger action potential firing in CeA neurons (Figure 4A). Although the EPSC amplitude is similar between the PKC-δ+ neurons and PKC-δ- neurons, fewer PKC-δ+ neurons (4 of 11 neurons) than PKC-δ- neurons (6 of 8 neurons) fired action potentials when the ChR2-expressing terminals were light stimulated (Figure 4B). If we consider only cells where action potentials were triggered, the successful action potential trigger rate is similar between these two populations (Figure 4C). Interestingly, the PKC-δ- neurons show an adaptation in action potential triggering when stimulated at 10 Hz, whereas PKC-δ+ neurons do not (Figure S2). We then plotted the success rate of action potential triggering against the EPSC amplitude of the neurons. We found that a larger-amplitude EPSC is required to trigger action potentials in CeA PKC-δ+ neurons than in PKC-δ- neurons (Figure 4D). Similar results were also observed in late firing neurons and regular spiking neurons (Figures 4E–4G). The different action potential triggering rates are consistent with their electrophysiological properties, i.e., the PKC-δ+ neurons or late firing neurons have a longer firing delay and therefore are more difficult to be triggered to fire action potentials. However, these results do not support the idea that CeA PKC-δ+ neurons are more likely to be activated when the insula-CeA pathway is light stimulated and cannot explain why activation of the pathway suppresses food intake.

Using Mathematical Modeling to Explore the Functional Connectivity Structure of the CeA Circuit

Experimental findings to be included in the model:

Finding 1

The PKC-δ+ and Htr2a+ neural populations in mice have similar electrophysiological properties, although they play opposite roles in feeding. The majority of these cells are late firing neurons in both populations (Cai et al., 2014; Douglass et al., 2017).

Finding 2

Activating only the PKC-δ+ population leads to feeding suppression, whereas silencing this population leads to feeding promotion in a fed state (Cai et al., 2014).

Finding 3

Activating only the Htr2a+ population, which is a subset of the PKC-δ- population, leads to feeding promotion, whereas silencing this population (or silencing the PKC-δ- population) leads to feeding suppression (Cai et al., 2014; Douglass et al., 2017).

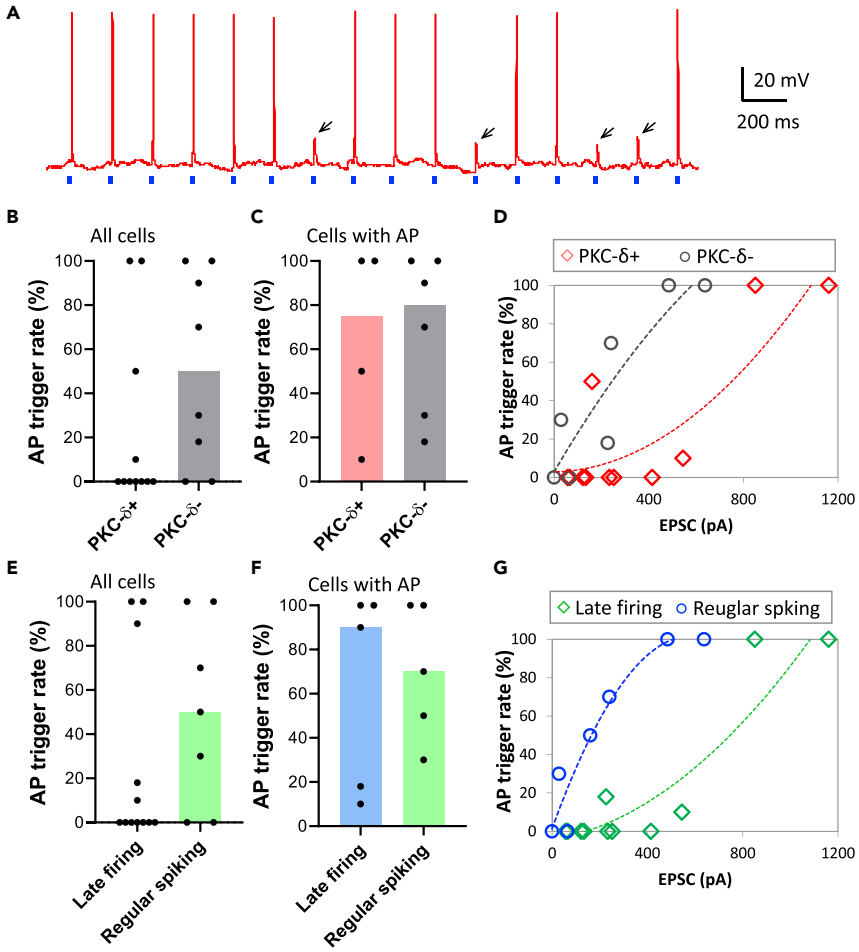

Figure 4. Activation of Insular Terminals in CeA Triggers Action Potential Firing in CeA Neurons

(A) Sample trace of current-clamp recording shows that action potential (AP) firing is triggered by 2-ms light pulses (blue dots). Note some light pulses cannot trigger action potential but a subthreshold depolarizing potential (indicated by arrows).

(B and C) Successful AP trigger rate in all the neurons (B) or neurons that at least one action potential is triggered (C). Bar graphs show median value. Each dot represents one cell.

(D) AP trigger rate is plotted against EPSC amplitude in PKC-δ+ neurons and PKC-δ- neurons. The dotted lines are polynomial fitting. Bar graphs show median value. Each data point represents one cell.

(E–F) Successful AP trigger rate in all the neurons (E) or neurons that at least one action potential is triggered (F). Bar graphs show median value. Each dot represents one cell.

(G) AP firing rate is plotted against EPSC amplitude in late firing neurons and regular spiking neurons. The dotted lines are polynomial fitting. Bar graphs show median value. Each data point represents one cell.

Finding 4

Surprisingly, activating both the PKC-δ+ and PKC-δ- population, which includes Htr2a+ neurons, through insular terminals consistently leads to feeding suppression (Figures 1E and 1F).

The first three findings imply intuitively the following functional structure of the CeA circuit: the PKC-δ+ and Htr2a+ populations act in functionally opposite ways; PKC-δ+ leads to feeding suppression when activated, whereas Htr2a+ leads to feeding promotion when activated. However, given that these two populations are functionally opposing each other and share similar electrophysiological properties (Cai et al., 2014; Douglass et al., 2017; Haubensak et al., 2010), it is not clear how this functional structure can produce the outcome observed in Finding 4, in which the simultaneous activation of both the PKC-δ+ and Htr2a+ populations leads consistently to a winner-take-all situation where PKC-δ+ is *always* the dominating population, resulting in a net effect of feeding suppression. It is known that winner-take-all can occur through symmetry-breaking pitchfork

bifurcation (Curtu et al., 2008; Werner and Spence, 1984); if so, the initial condition (and noise) would play a critical role in determining which of the two neural populations becomes the dominating one. A pair of identical and mutually inhibitory neuronal populations cannot *consistently* produce an outcome in which one particular population is always dominating the other as observed in Finding 4 (Rowat and Selverston, 1997; Shpiro et al., 2007). If we relax the assumption that these two populations are identical, such as by allowing for a sufficient amount of asymmetry between the two populations, then the winner-take-all outcome of Finding 4 can occur consistently (more on this later). However, existing experimental evidence does not suggest such strong asymmetry between the LF1 and LF2 populations (Cai et al., 2014; Douglass et al., 2017; Haubensak et al., 2010). A question arises: is it possible that a third population of neurons consisting of regular spiking neurons, most of which are negative for either PKC-δ or Htr2a (Cai et al., 2014; Douglass et al., 2017), plays a functionally significant role as part of the overall CeA circuit in modulating feeding behavior?

To reconcile the existing results and to compare various possible CeA circuit structures, we consider a simple neuronal network model of the CeA circuit consisting of three distinct CeA neurons: a late firing neuron (LF1) representing the PKC-δ+ neural population, another late firing neuron (LF2) representing either the Htr2a+ population or a subset of the PKC-δ- population, and possibly a third neuron that is regular spiking (RS) as another subset of the PKC-δ- population. Existing findings suggest that synaptic connections within the CeA circuit are inhibitory (Haubensak et al., 2010; Hou et al., 2016; Hunt et al., 2017; Sun and Cassell, 1993) and that the LF1 PKC-δ+ and LF2 PKC-δ-/Htr2a+ neurons are mutually inhibitory (Cai et al., 2014; Douglass et al., 2017; Haubensak et al., 2010). Hence, in this study we only allow for variations in the inhibitory synaptic connections from the third RS neuron to the two LF neurons as shown in Figure 5A. Given the above assumptions, we need to consider four network connectivity scenarios shown in Figures 5B–5E. Note that Figure 5B is the special case in which the RS neuron is absent. To explore the functional significance of the regular spiking or late firing properties of the individual CeA neurons, we also consider variations in the electrophysiological properties of the three CeA neurons, such as the third neuron being late firing instead of regular spiking, as shown in Figure 5C′, 5D′, and 5E′, or the scenarios in which the LF1 (representing PKC-δ+) and LF2 (representing PKC-δ-/Htr2a+) neurons are regular spiking instead of late firing, as shown in Figures $5D^1$, $5D^2$, and $5D^3$. Analyzing these alternatives allows us to address whether the late firing property of the PKC-δ+ and Htr2a+ populations, and possibly the presence of a third regular spiking subpopulation, is a necessary condition for the observed CeA circuit output behaviors.

Based on the CeA circuit structure proposed above, we develop a dynamical systems model of neuronal activity in the CeA circuit in which each of the three CeA neurons is represented by a Hodgkin-Huxley-type model neuron that produces the desired electrophysiological property (i.e., late firing or regular spiking) in each scenario (see Transparent Methods). We use an idealized conductance-based current model for the inhibitory synaptic connections with time-dependent channel dynamics mimicking the general behavior of GABA channels. Each model neuron receives an external input, which represents the activation input from the insular cortex; the external input is positive when the activation input is on and negative when the neuron is silenced. The resulting mathematical model of the entire CeA circuit is a system of differential equations with about 19 dynamic variables (the exact number of variables in each scenario varies and depends on the exact combination of the electrophysiological properties of the individual CeA neurons and the overall network connectivity scenario). Note that we do not consider the effect of heterogeneity within each CeA neural population in this article. In future work, we shall consider the heterogeneous case.

Finally, we describe how the CeA circuit output is linked to feeding behavior in our model. Findings 2 and 3 suggest the following simple model on the effect of the CeA circuit output on feeding behavior: the firing rate of LF1 neuron (representing the PKC-δ+ population) is proportional to the strength of feeding suppression, and the firing rate of LF2 neuron (representing the Htr2a+ population) is proportional to the strength of feeding promotion. We assume that the activity of RS neuron does not have a direct influence on feeding behavior. Consistent with our modeling principle of using the fewest assumptions possible, our model supposes that the negative effect on feeding exerted by LF1 and the positive effect by LF2 sum up linearly, and this sum provides a quantitative measure of the net effect of the CeA circuit output on feeding.

A Third Regular Spiking Subpopulation of Neurons Are Functionally Significant for Producing the Desired CeA Circuit Dynamics

Among the circuit scenarios shown in Figures 5B, 5C, 5C′, 5D, 5D′, 5E, and 5E′, we found only one specific CeA circuit structure capable of reproducing all four experimental findings. Figure 5D shows this

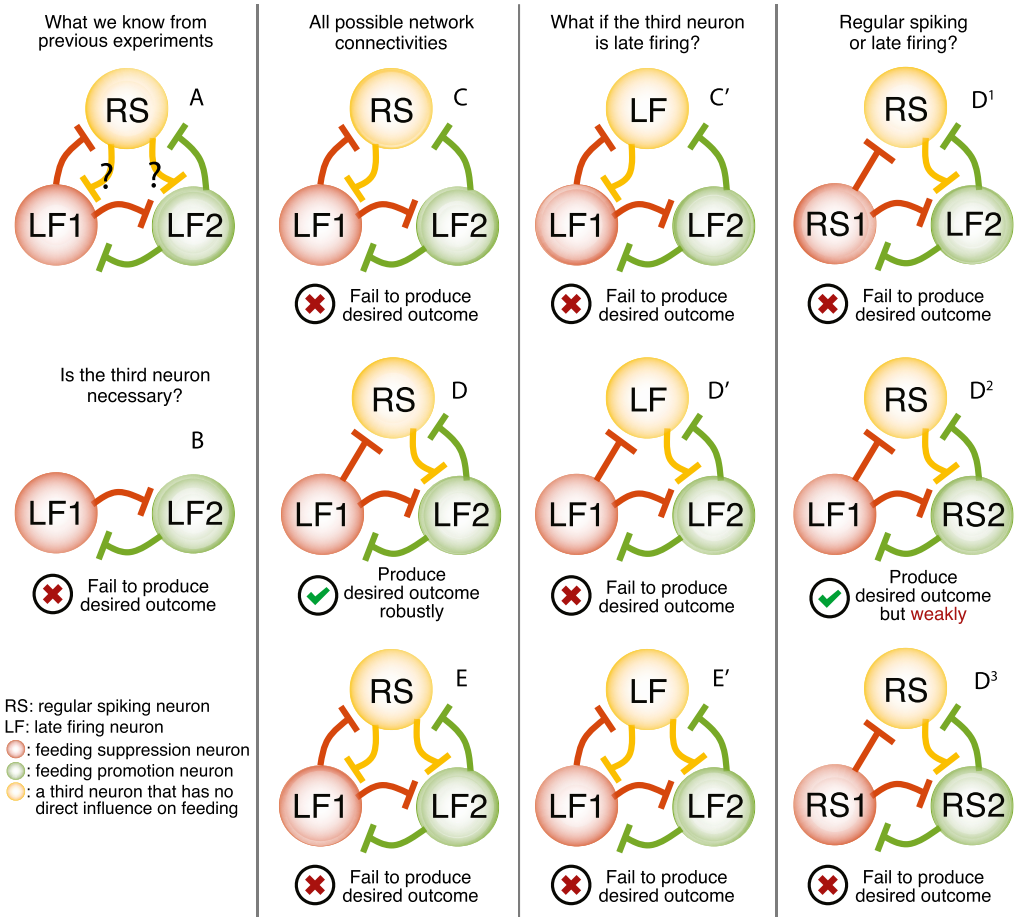

Figure 5. Various Hypothetical Circuit Structures for the CeA Circuit

We consider various combinations of connectivity topologies and intrinsic firing properties for the CeA circuit consisting of three CeA model neurons. Based on the model assumptions discussed in the Results section, symmetry analysis implies only nine fundamentally different scenarios (including the degenerated case with only two neurons, in which the third CeA neuron with no direct influence on feeding is absent). Computer simulations of our mathematical model of this CeA circuit shows that only the CeA circuit structure proposed in subfigure A is able to reproduce all previously observed feeding behavior change in response to various experimental conditions (see Figure 6 for the computer simulation results of this scenario). Parameter values used in the computer simulations: $\overline{g}_K = 36$ mS/cm^2, $\overline{g}_{Na} = 120$ mS/cm^2, $g_L = 0.3$ mS/cm^2, $\overline{g}_A = 50$ mS/cm^2, $\overline{g}_{ij}^{syn} = 5$ mS/cm^2 for all neurons, $E_K = -77$ mV, $E_{Na} = 50$ mV, $E_L = -54.4$ mV, $E_{syn} = -70$ mV, $\tau_B = 16$ msec, $I_{bias} = 20$ mA, $I_i^{ext} = 20$ for activation, $I_i^{ext} = -60$ mA for silencing, $I_i^{ext} = 0$ for the control condition, and $C = 1$ μF/cm^2. Each simulation is run for 4,000 msec; we only use results from the last one-third of the time span to allow sufficient time for the stable activity to emerge from the initial transients.

successful CeA circuit structure, in which the RS neuron receives an inhibitory synaptic connection from LF1 and forms a mutually inhibitory synaptic connection with LF2, and therefore providing a disynaptic inhibitory pathway from LF1 to LF2 in addition to the existing mutual inhibition between the LF1 and LF2 neurons. The second column in Figure 6 shows the membrane potential time course of our three CeA neurons, using this CeA circuit structure, under various conditions. In the control condition (no additional external input to any of the three CeA neurons except for the baseline bias input), the extra disynaptic inhibitory pathway from LF1 via RS to LF2 breaks an otherwise perfect symmetry between LF1 and LF2, resulting in a firing pattern of 2:1–2:1–1:1 with LF1 firing more frequently than LF2. Intuitively, as we activate both LF1 and LF2 (by increasing the external drive to LF1 and LF2 but not to RS), the firing rates of both LF1 and LF2 become elevated, resulting in a net increase in the number of spikes fired by LF1 (since LF1 already fires more spikes than LF2 in the control condition). This net increase is further exacerbated by a change in the firing pattern of LF1 and LF2 from 2:1–2:1–1:1 to a persistent 2:1 ratio. Either of these two effects alone leads to a net increase in LF1 spikes, and therefore, activating both the LF1

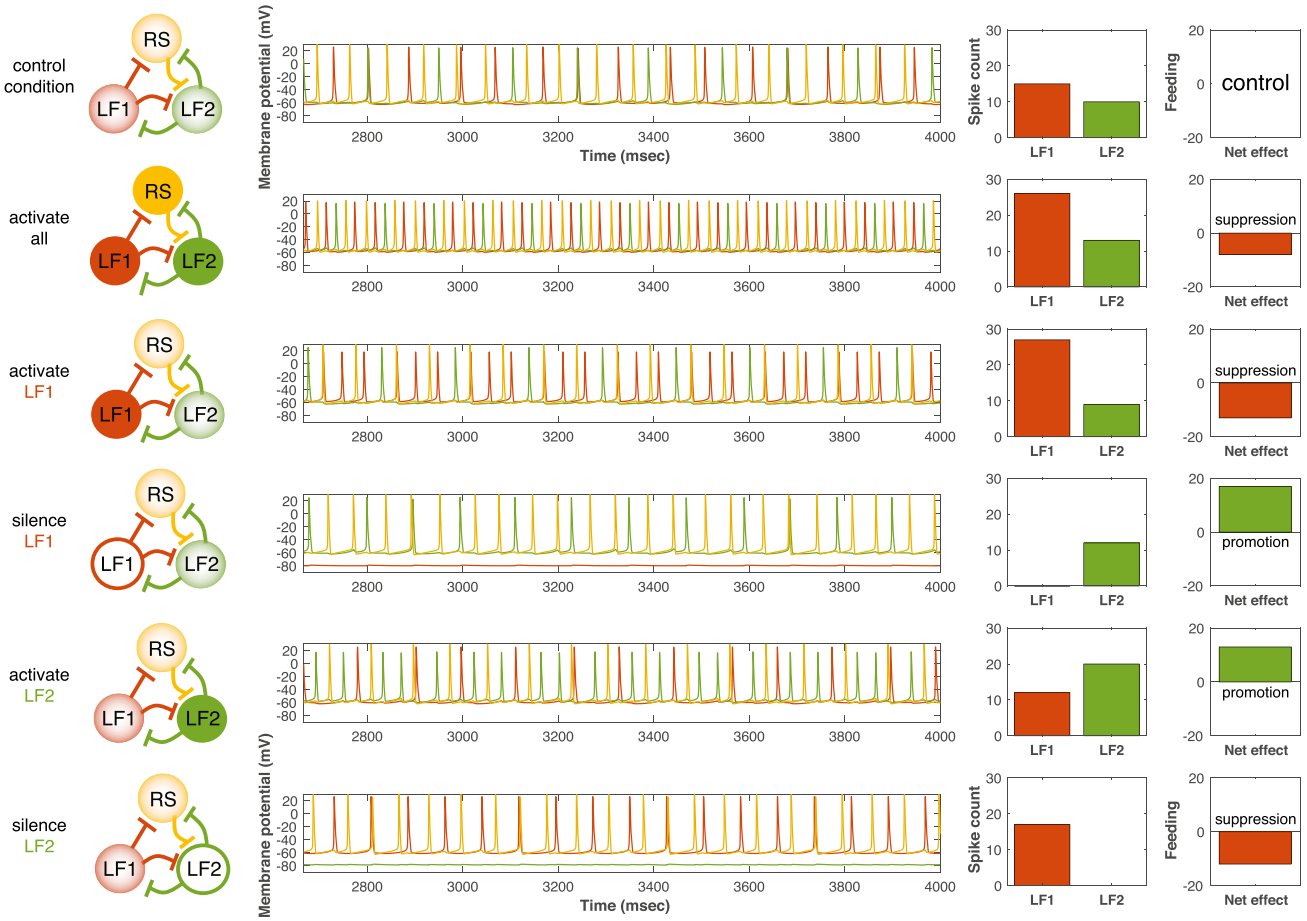

Figure 6. The Response of Our Proposed CeA Circuit Model to Various External Stimuli

We subject our proposed CeA circuit model (shown in Figure 5A) to five different conditions: activating all three model neurons ($I_{LF1}^{ext} = I_{LF2}^{ext} = I_{RS}^{ext} = 20$ mA), activating only the LF1 neuron ($I_{LF1}^{ext} = 20$ mA), silencing only the LF1 neuron ($I_{LF1}^{ext} = -60$ mA), activating only the LF2 neuron ($I_{LF2}^{ext} = 20$ mA), and silencing only the LF2 neuron ($I_{LF2}^{ext} = -60$ mA). The first column shows the five different conditions (in addition to the control condition shown in the first row) imposed on our CeA circuit model. Each circle represents a CeA model neuron; a solid color circle indicates activation, a hollow color circle indicates silencing, and a color circle with a color gradient indicates the control condition ($I_i^{ext} = 0$). The second column shows the membrane potentials of the three CeA model neurons as functions of time; the red curve for the LF1 neuron, the green curve for the LF2 neuron, and the yellow curve for the RS neuron. Each simulation is run for 1,000 msec. Note that the figure shows only the neuronal activities during the last one-third of the time span to allow sufficient time for the initial unstable transient activity to settle to a stable activity. The third column shows the spike count of the LF1 and LF2 neurons (during the last one-third of the time span). In the last column, we show the net effective of the CeA circuit firing activity on feeding behavior. Recall that, in our model, the firing rate of LF1 neuron is proportional to its effect on feeding suppression and the firing rate of LF2 neuron is proportional to its effect on feeding promotion, whereas the dynamics of the RS neuron has no direct effect on feeding behavior (the RS neuron indirectly influences the feeding behavior through its synaptic connections with the other two neurons). The net effect is obtained by subtracting the LF1 neuron spike count from the LF1 neuron spike count (we treat the control condition as the neutral case; the net spike count in the control condition provides the baseline for comparison). All model parameter values are the same as described in Figure 5 caption (except we use a longer time span here for illustration purposes).

and LF2 neurons results in feeding suppression. This result is shown in the second row in Figure 6. The third row of Figure 6 shows that the activation of LF1 leads to feeding suppression; in this case, an elevated LF1 neuron leads to an increased inhibition to LF2, resulting in a 3:1 ratio in the firing rate of LF1 over LF2. The fourth row in Figure 6 shows the opposite case in which LF1 is silenced; in this case, the LF2 and RS neurons become the only active neurons, resulting in feeding promotion. The fifth row reproduces the result that LF2 activation leads to feeding promotion; the elevated activity of LF2 leads to a reversal in the firing rate ratio of LF1 over LF2 from the 2:1–2:1–1:1 pattern (control condition) to the 1:2–1:2–1:1 pattern, resulting in a net increase in the number of spikes of LF2, and therefore producing a net effect of feeding promotion. In the last row, as we silence only the LF2 neuron, LF1 and RS become the only active neurons, resulting in feeding suppression.

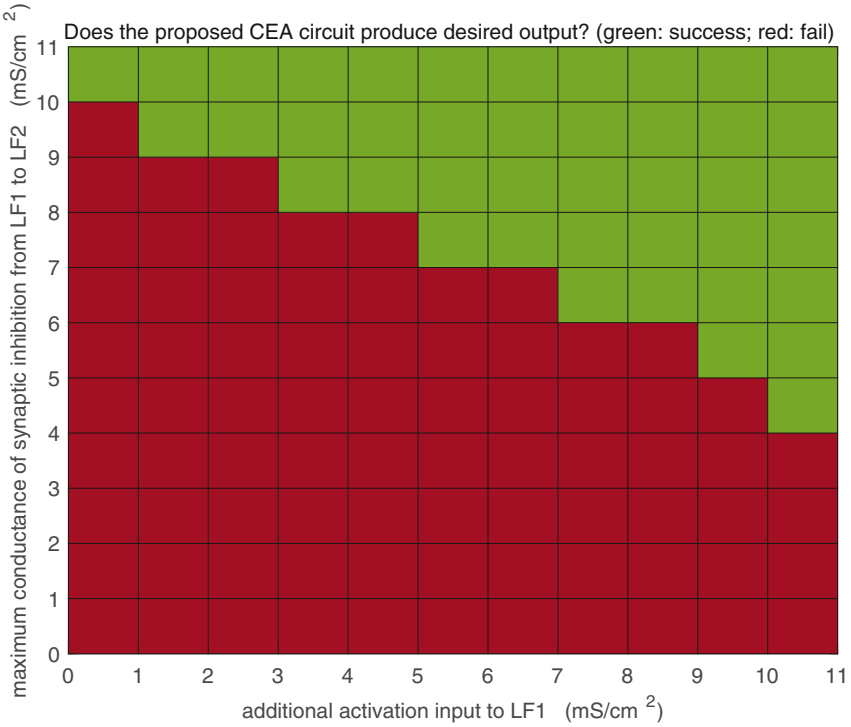

Figure 7. Effect of Asymmetry in the Two-Cell LF1-LF2 Network

Computer simulations of the two-cell network (LF1-LF2) with varying degrees of asymmetry. We introduce asymmetry to the two-cell network by adjusting two parameters: (1) the maximum conductance of the synaptic inhibition from LF1 to LF2 (introducing an asymmetry in the mutual inhibition between LF1 and LF2) and (2) an extra external current input to the LF1 neuron (introducing an asymmetry in the insular cortex inputs to LF1 and LF2). For each combination of parameter values, we run a series of computer simulations under the same five experimental conditions (as in Figure 6) to test whether the CeA circuit being tested can reproduce all desired CeA circuit output outcomes. If successful (i.e., all desired outcomes are reproduced), a green block is plotted at the location corresponding to the parameter combination, and if unsuccessful (i.e., at least one desired outcome is not reproducible), a red block is plotted. All other parameters values are the same as described in Figures 5 and 6 captions. In all computer simulations, in order to declare an outcome as feeding suppression, we require that the number of LF1 spikes to be at least three more than the number of LF2 spikes, whereas to declare an outcome as feeding promotion, we require that the number of LF2 spikes be at least three more than the number of LF1 spikes.

We then consider several alternative circuit structures. We first ask what would happen if the regular spiking neural population was absent. In this case, the original three-cell CeA circuit is reduced to a pair of mutually inhibitory late firing neurons as shown in Figure 5B. This symmetric mutual inhibitory structure gives rise to identical firing rate in both the LF1 and LF2 neurons. Not surprisingly, this scenario is able to reproduce experimental Findings 2 and 3, in which LF1 or LF2 is either activated or silenced. However, when both LF1 and LF2 are activated, the net effect on feeding is nil, since the elevated suppressing effect of LF1 is canceled out perfectly by an equally elevated promoting effect of LF2. This outcome is a consequence of our model assumption that the LF1 and LF2 neurons are identical and that the two neurons are coupled through mutual inhibition with equal strength. However, if we allow for a sufficient amount of asymmetry between LF1 and LF2, it is possible that the winner-take-all outcome observed in Finding 4 can occur. To see how much asymmetry is needed to reproduce Finding 4, we introduce two types of asymmetry between LF1 and LF2: (1) an asymmetry in the strength of the activation input to each neuron and (2) an asymmetry in the mutual inhibition between the two neurons. Results are shown in Figure 7. We find that, in order to produce all the desired outcomes, including the winner-take-all outcome required by Finding 4, either the maximum conductance of the synaptic inhibition from LF1 to LF2 has to be at least twice that from LF2 to LF1 or the external current input into LF1 has to be at least twice that into LF2. This result suggests that, in order for a two-cell (both late firing) network to produce all the desired firing-rate behaviors, a strong asymmetry between the LF1 and LF2 populations is needed. However, existing experimental evidence does not suggest such strong asymmetry between the LF1 and LF2 populations (Cai et al., 2014; Douglass et al., 2017; Haubensak et al., 2010).

We continue to consider additional alternative connectivity scenarios. In Figure 5C, the RS neuron is bidirectionally coupled to LF1 via mutual inhibition; in Figure 5E, we consider a fully coupled network of LF1, LF2, and RS neurons, in which each neuron forms a mutual inhibition with the other two neurons; and in Figures 5C′, 5D′, and 5E′, the RS neuron is replaced by a third LF neuron. Computer simulations show that none of the above alternative scenarios is able to reproduce all of the existing experimental findings. Specifically, the alternative scenarios may reproduce Findings 2 and 3 but fail to reproduce Finding 4. This suggests that the third regular spiking neuronal population plays a functionally significant role in modulating CeA circuit output and that this modulation is in the form of an inhibitory pathway from the PKC-δ+ population to the regular spiking population and finally to the Htr2a+ population.

The Late Firing Property of the CeA Neurons Is Necessary to Produce the Experimentally Observed Behaviors

We have identified a specific CeA circuit structure that reproduces qualitatively all of the four experimental findings. In particular, our proposed CeA circuit structure (Figure 5D) consists of three neural populations, in which a mutually inhibitory pair of late firing neurons represents the PKC-δ+ population (LF1) and the Htr2a+ population (LF2), respectively, and a third regular spiking neural population inserts an additional inhibitory pathway from LF1 to LF2. Our model is consistent with the experimental finding that both the PKC-δ+ and Htr2a+ populations are mostly late firing neurons (Douglass et al., 2017; Haubensak et al., 2010). This raises another interesting question: is the late firing property of CeA neurons (represented by LF1 and LF2 neurons in our model) a necessary electrophysiological condition for the CeA circuit to produce the experimentally observed behaviors under various experimental conditions?

To address this question, we use our mathematical model to further explore various alternative scenarios by modifying the prescribed electrophysiological property of the PKC-δ+ and Htr2a+ populations in our model: in Figure 5D^1, we consider the case in which the PKC-δ+ neural population is regular spiking (instead of late firing); in Figure 5D^2, we consider the case in which the Htr2a+ population is regular spiking (instead of late firing); and in Figure 5D^3, we consider the case that both the PKC-δ+ and Htr2a+ neurons are regular spiking. Computer simulations show that scenarios D1 and D^3 fail to reproduce Finding 4 (that the activation of both PKC-δ+ and PKC-δ- neurons should lead to feeding suppression), whereas scenario D^2 is able to reproduce the desired outcome but in a weak manner (in the sense that the feeding suppression effect when both the PKC-δ+ and Htr2a+ populations are activated is much weaker than the suppression effect under the condition when only the PKC-δ+ population is activated). This result implies that the late firing property of the PKC-δ+ and Htr2a+ neurons is essential to ensure the desired feeding behavior. Note that a key feature of our model is that the regular spiking neuron does not have a direct influence on feeding behavior; however, the regular spiking neuron *does* have an indirect effect on the neuronal activity of the CeA circuit and its effect on other populations, and therefore, our result also suggests that the regular spiking property of the third neural population is also necessary to achieve the desired CeA circuit output behaviors.

To test the robustness of our modeling results against variations in the strength of synaptic connections between the CeA neurons, we performed a two-dimensional numerical bifurcation study to examine how the solutions of our dynamical systems model for the CeA circuit change as we vary the values of the parameters $\overline{g}_{ij}^{syn}$, the strength of the synaptic connection from neuron j to neuron i. Specifically, we vary the values of two types of synaptic connections, those originating from the late firing neurons and those originating from the regular spiking neuron. We reran our computer simulations for various combinations of these two synaptic strength values and tested each case to verify whether all desired outcomes are satisfied. Figures 8A and 8B show the bifurcation study results for our proposed CeA circuit (as shown in Figure 5D) and the weak scenario as shown Figure 5D^2. A green color block indicates that all desired findings can be reproduced under this specific parameter combination, whereas a red color block indicates at least one of the desired outcomes is violated. Our result shows that our proposed CeA circuit is able to reproduce all desired outcomes over a wide range of synaptic strength combinations, whereas the weak scenario has a smaller area of green blocks. Overall, this bifurcation study shows that our main conclusions from the mathematical model is robust against variations in synaptic strength.

DISCUSSION

Neurons in the CeA have been widely reported to play important roles in fear conditioning, anxiety, pain, reward processing, and feeding behaviors (Duvarci et al., 2011; Fadok et al., 2018; Gilpin et al., 2015; Janak

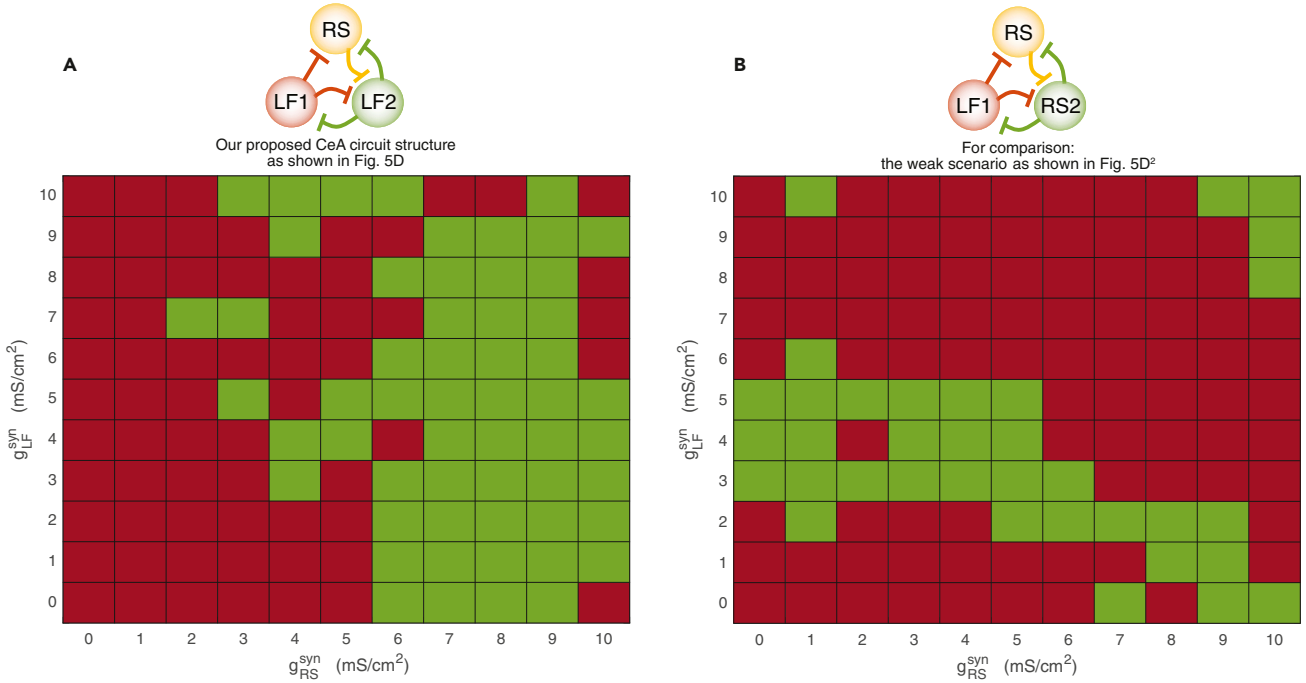

Figure 8. Robustness of Our Mathematical Model Results against Variations in Synaptic Strength

For each combination of synaptic strength values, we run a series of computer simulations under the same five experimental conditions (as in Figure 6) to test whether the CeA circuit being tested can reproduce all desired CeA circuit output outcomes. Using the same notation and criteria as described in Figure 7 caption, if successful, a green block is plotted at the location corresponding to the parameter combination, and if unsuccessful, a red block is plotted. For comparison, we perform this two-dimensional numerical bifurcation study for two CeA circuit scenarios: in (A), we test the scenario shown in Figure 5D (i.e., our proposed CeA circuit structure); in (B), we test the scenario shown in Figure 5D^2 (i.e., the scenario that produces only a weak outcome of feeding suppression when both the PKC-δ+ and Htr2a+ populations are activated). The parameter $\overline{g}^{syn}_{LF}$ is the catch-all variable for all maximum conductance parameters $\overline{g}^{syn}_{ij}$ in which the presynaptic neuron *j* is late firing (regardless of the postsynaptic neuron *i*), whereas $\overline{g}^{syn}_{RS}$ is the catch-all variable for all $\overline{g}^{syn}_{ij}$ in which the presynaptic neuron *j* is regular spiking (regardless of the postsynaptic neuron *i*). All other parameters values are the same as described in Figures 5 and 6 captions.

and Tye, 2015; Johansen et al., 2011; LeDoux, 2000; Ressler and Maren, 2019; Thompson and Neugebauer, 2017). Accordingly, it is not surprising that many different types of CeA neurons were identified based on their distinct electrophysiological properties, neuropeptides, or other genetic markers (Day et al., 1999; Dumont et al., 2002; Haubensak et al., 2010; Kim et al., 2017; van den Burg and Stoop, 2019). Recent studies using genetic marker-labeled CeA neurons revealed several subpopulations of CeA neurons with different functions in feeding regulation (Cai et al., 2014; Douglass et al., 2017; Hardaway et al., 2019; Ip et al., 2019; Kim et al., 2017). Especially, two non-overlapping CeA neurons, marked by the expression of PKC-δ+ and Htr2a+, respectively, were identified to regulate feeding in opposing directions (Cai et al., 2014; Douglass et al., 2017). Activation of CeA PKC-δ+ neurons suppresses food intake, whereas activation of CeA Htr2a+ neurons increases food intake. Activation of CeA PKC-δ- neurons does not seem to affect food intake significantly, despite the Htr2a+ population being included in this subset (Cai et al., 2014; Douglass et al., 2017). Silencing CeA PKC-δ+ neurons increases food intake, but silencing CeA PKC-δ- neurons or silencing CeA Htr2a+ neurons decreases food intake (Cai et al., 2014; Douglass et al., 2017). Surprisingly, a majority of the CeA PKC-δ+ neurons (86%) or Htr2a+ neurons (85%) in mice are late firing neurons (Cai et al., 2014; Douglass et al., 2017), suggesting that the distinct functions of these two populations are not purely a result of their electrophysiological properties. Neurons in the CeA receive inputs from diverse brain regions, some of which have been demonstrated to regulate behaviors related to feeding (Campos et al., 2016; Palmiter, 2018; Schiff et al., 2018; Wang et al., 2018). For example, it was reported that neurons in the lateral parabrachial nucleus (LPB) that express calcitonin gene-related protein (CGRP) relay danger information and project to the CeA to suppress food intake (Campos et al., 2018; Carter et al., 2013); neurons in insular cortex that encode bitter taste project to CeA to convey negative valence (Schiff et al., 2018; Wang et al., 2018). More recently, Gehrlach et al. expressed ChR2 in insular cortex under *CamK2a* promoter and demonstrated that activation of the insula→CeA pathway suppresses feeding, increases anxiety, and

induces other aversive behaviors (Gehrlach et al., 2019). Interestingly, when we used AAVretro-Cre in CeA and Cre-dependent ChR2 in insular cortex, we only observed feeding suppression but not anxiety or other aversive behaviors. This might reflect a weaker activation of insular cortex neurons; either a smaller number of neurons or a lower expression of ChR2 in the insular cortex could achieve a manipulation more specific to a certain behavior. This possibility was also supported by Gehrlach's finding that a higher-frequency (20 Hz) stimulation triggers immobility and many aversive behaviors, whereas a lower frequency (10 Hz) does not (Gehrlach et al., 2019). Stern et al. recently found that inhibition of the projection from insular cortex Nos1 neurons to CeA has no effect on normal feeding but blocks the context conditioned overconsumption; however, the connections from Nos1 neurons to different CeA neurons were not directly mapped (Stern et al., 2019). Retrograde rabies tracing studies showed that both the CeA PKC-δ+ and CeA PKC-δ- neurons receive monosynaptic inputs from many common brain regions including insular cortex and LPB (Cai et al., 2014; Douglass et al., 2017). Here our results demonstrate that neurons from insular cortex send monosynaptic excitatory inputs to all the CeA neurons non-selectively. The synaptic strength is not significantly different between CeA PKC-δ+ neurons and CeA PKC-δ- neurons or between late firing neurons and regular spiking neurons. It seems that the CeA PKC-δ+ neurons require a larger EPSC to activate them than the CeA PKC-δ- neurons. Thus, it is surprising that activation of the neural pathway from insular cortex to CeA suppresses food intake, an effect similar to the activation of CeA PKC-δ+ neurons or silencing CeA PKC-δ- neurons. Therefore, the different functions of CeA neurons cannot be explained by their inputs either. Instead, these results suggest that the distinct functions of the CeA neurons might be due to their special circuit structure within CeA.

The functional connections among the CeA neurons have been recently studied using two different strategies. One is based on the ChR2-assisted circuit mapping, in which ChR2 is expressed in a subtype of CeA neurons with specific genetic markers and postsynaptic responses of other CeA neurons are recorded in response to light stimulation of the ChR2-expressing neurons. It was found that almost all the CeA PKC-δ- neurons receive monosynaptic inhibition from CeA PKC-δ+ neurons (Haubensak et al., 2010) and almost all CeA Htr2a negative (CeA Htr2a-) neurons are inhibited by light activation of the CeA Htr2a+ neurons (Douglass et al., 2017). Similarly, almost all CeA somatostatin (SOM) negative (CeA SOM-) neurons are inhibited by CeA SOM+ neurons (Hunt et al., 2017; Li et al., 2013). These studies indicate that CeA neurons form extensive inhibition with each other at the population level. The other strategy is based on paired whole-cell recording and stimulation on individual neurons, which also showed extensive interconnections among all electrophysiological types of CeA neurons (Hou et al., 2016; Hunt et al., 2017). Both unidirectional and bidirectional connections between late firing neurons, from late firing to regular spiking neurons and from regular spiking to late firing neurons, were observed (Hunt et al., 2017; Li et al., 2013). However, current available genetic markers cannot label all the different types of CeA neurons. For example, what genetic marker may label regular spiking neurons is still unknown and the role of regular spiking neurons in feeding remains to be determined. The paired recording cannot detect the connections between cells that are far away from each other or cells located in different brain slices, and the number of cells that can be sampled with this method is usually limited. Therefore, it is difficult to measure the exact connections among different types of CeA neurons that have distinct functions with current technologies.

Although current experiments cannot tease out the exact CeA circuit connectivity, mathematical modeling is powerful in testing all possible network structures based on current knowledge of CeA neurons (functions, electrophysiological properties, and connections) to explore which specific neuronal network can produce the experimentally observed results. Constrained by existing experimental findings, we have built a conductance-based model for each type of CeA neurons using Hodgkin-Huxley-type equations and used it to explore how the firing properties of individual CeA neurons and the CeA circuit's overall synaptic organization combine to produce the desired circuit output for feeding control. Computer simulations of our mathematical model show that, in order to produce the experimentally observed feeding behaviors in response to various conditions, the presence of both late firing and regular spiking neurons are necessary. Furthermore, by examining different combinations of circuit connectivity scenarios, we find one specific CeA circuit synaptic organization that can reproduce previously known experimental findings. An important outcome of our CeA circuit model is that, at the control condition, the LF1 neuron (representing the PKC-δ+ population) has a higher firing rate than the LF2 neuron (representing the PKC-δ- or Htr2a+ population) (Ciocchi et al., 2010), so that the activation of both CeA populations (such as by the activation of insular cortex neurons) would lead to a net increase in the spikes fired by the LF1 neurons, which leads to feeding suppression according to our model assumption.

Note that, however, our proposed three-neuron structure is not necessarily the only possible structure to achieve the desired outcome. The necessity of a third regular spiking neuron is a consequence of our model assumption that the two late firing LF1 and LF2 neurons are identical and that these two neurons are coupled through mutual inhibition with equal strength. This result shows the potential functional significance of having a mixture of late firing and regular spiking neurons.

We would like to point out some limitations of our mathematical model. First, our CeA circuit model consists of three Hodgkin-Huxley-type model neurons, each of which represents a CeA neural population. Therefore, our model is not a population model and cannot address heterogeneity within each CeA neural population or subregions of CeA or even outputs of the CeA neurons; in future work, we shall consider population models, such as Wilson-Cowan-type models (Destexhe and Sejnowski, 2009; Wilson and Cowan, 1973) or models based on large dynamical systems (Rangan and Young, 2013) that can take into account the heterogeneity within each CeA neural population. Second, the delayed onset firing property of our late firing CeA model neuron is implemented by the incorporation of a potassium A-type current, which is a fast-activation and slow-inactivation outward current (Rush and Rinzel, 1995). Other dynamical mechanisms, such as those caused by a slow calcium buildup (Rush and Rinzel, 1995; Terman et al., 2002), can also lead to a delayed-onset firing, which we did not consider in our model. Third, our model does not consider long-term adaptations in the synaptic connections except our model includes time-dependent synaptic dynamics to account for the general behavior of GABA channels. It is possible that synaptic strength adapts to feeding behavior through certain feedback pathways, which requires further experiments to determine. Fourth, our model assumes that the firing rate of the LF1 neuron is linearly proportional to the strength of feeding suppression, and the activity of LF2 is linearly proportional to the strength of feeding promotion, and that these two effects add up linearly to give the net effect of the CeA circuit on feeding. We do not consider gain control mechanism or nonlinearity in our model. We did so because we aimed to use the fewest assumptions that are consistent with the existing experimental observations. The main feature of our CeA circuit model is that the feeding suppressing effect of the LF1 neuron directly competes with the feeding promoting effect of the LF2 neuron, and this competition is modulated by the mutual inhibition between these two late firing neurons, and at the same time, by the extra inhibitory pathway from the LF1 neuron through the RS neuron to the LF2 neuron.

Although the actual connections within the CeA are still unknown, using computational modeling, we found that a specific circuit structure, combined with the intrinsic electrophysiological properties of the CeA neurons, can explain the puzzling feeding-related results. This circuit diagram can provide a platform for identifying specific types of CeA neurons involved in regulating feeding and other behaviors such as fear conditioning and pain (Haubensak et al., 2010; Isosaka et al., 2015; Wilson et al., 2019). From a broader perspective, a large amount of modeling work has studied the dynamics of individual conductance-based model neurons and the networks formed by these neurons (Izhikevich, 2007), such as in the stomatogastric ganglion (Selverston, 2008), the crayfish swimmeret system (Skinner and Mulloney, 1998; Zhang et al., 2014), and the hippocampus (Rich et al., 2016). However, to the authors' knowledge, no previous study has examined the dynamics of a neural circuit consisting of at least two mutually inhibitory neurons in which one is regular spiking and the other is late firing. Hence, it is possible that the circuit structure and the underlying mechanism identified herein may be more broadly applicable.

Limitations of the Study

In the feeding study, we used a combination of viruses, AAVretro-Cre in CeA and Cre-dependent ChR2 in insular cortex, to manipulate the insula → CeA pathway. Although the generality of retrograde transport of AAVretro has been well established, it is still possible that a subset of the insula-CeA projections is preferentially transduced and activated in this study. Because we did not observe obvious anxiety or aversive behaviors that was observed in studies where ChR2 was expressed in insular cortex neurons under *CamK2a* promoter, our results suggest that the insula-CeA neural pathways might be heterogeneous and are involved in multiple functions. Another limitation is that our electrophysiological studies that demonstrate the insula-CeA connections and their synaptic strength are performed in *ex vivo* brain slice, in which many connections are lost. An important open question is whether these connections are the same when the circuit structure is intact.

Our mathematical model for the CeA neuronal circuit is a simple conductance-based network model consisting of three Hodgkin-Huxley-type model neurons, each of which represents a CeA subpopulation.

Hence, our model is not a population model and cannot take into consideration the heterogeneity within each CeA subpopulation. Nevertheless, we believe that our result on the functional necessity of both late firing and regular spiking neurons may be generally applicable to more complex models.

Despite these limitations, our study demonstrated that both the circuit structure within CeA and the electrophysiological properties of the CeA neurons play critical roles in shaping their function.

METHODS

All methods can be found in the accompanying Transparent Methods supplemental file.

DATA AND CODE AVAILABILITY

Requests for further information or biological data and reagents should be directed to and will be fulfilled by Haijiang Cai (haijiangcai@email.arizona.edu). Request for numerical simulation code should be directed to and will be fulfilled by Calvin Zhang-Molina (calvinz@math.arizona.edu).

SUPPLEMENTAL INFORMATION

Supplemental Information can be found online at https://doi.org/10.1016/j.isci.2020.101033.

ACKNOWLEDGMENTS

We thank W. Haubensak and D. Anderson for PKC-δ-Cre mice; K. Deisseroth and E. Boyden for viruses; C. Fang for managing mice colony and genotyping; and K. Gothard and S. Cowen for comments and critical reading of the manuscript. Part of the brain slice electrophysiology experiments were carried out in the laboratory of Dr. D. Anderson (California Institute of Technology). H.C. is supported by a NARSAD Young Investigator Grant from the Brain & Behavior Research Foundation, Gant ID 25304, a grant from the Foundation for Prader-Willi Research, Grant ID 647545, and a grant from The Klarman Family Foundation Eating Disorders Research Grants Program, Grant ID 4770.

AUTHOR CONTRIBUTIONS

C.Z.-M. performed mathematical modeling and computer simulations, M.B.S. performed behavioral experiments, and H.C. performed electrophysiology experiments. C.Z.M., M.B.S., and H.C. wrote the paper.

DECLARATION OF INTERESTS

The authors declare no competing interests.

Received: August 28, 2019
Revised: January 2, 2020
Accepted: March 31, 2020
Published: April 24, 2020

REFERENCES

Accolla, R., and Carleton, A. (2008). Internal body state influences topographical plasticity of sensory representations in the rat gustatory cortex. Proc. Natl. Acad. Sci. U S A *105*, 4010–4015.

Andermann, M.L., and Lowell, B.B. (2017). Toward a wiring diagram understanding of appetite control. Neuron *95*, 757–778.

Augustine, J.R. (1996). Circuitry and functional aspects of the insular lobe in primates including humans. Brain Res. Rev. *22*, 229–244.

Cai, H., Haubensak, W., Anthony, T.E., and Anderson, D.J. (2014). Central amygdala PKC-delta(+) neurons mediate the influence of multiple anorexigenic signals. Nat. Neurosci. *17*, 1240–1248.

Campos, C.A., Bowen, A.J., Roman, C.W., and Palmiter, R.D. (2018). Encoding of danger by parabrachial CGRP neurons. Nature *555*, 617–622.

Campos, C.A., Bowen, A.J., Schwartz, M.W., and Palmiter, R.D. (2016). Parabrachial CGRP neurons control meal termination. Cell Metab. *23*, 811–820.

Carter, M.E., Soden, M.E., Zweifel, L.S., and Palmiter, R.D. (2013). Genetic identification of a neural circuit that suppresses appetite. Nature *503*, 111–114.

Caruana, F., Jezzini, A., Sbriscia-Fioretti, B., Rizzolatti, G., and Gallese, V. (2011). Emotional and social behaviors elicited by electrical stimulation of the insula in the macaque monkey. Curr. Biol. *21*, 195–199.

Chen, X., Gabitto, M., Peng, Y., Ryba, N.J., and Zuker, C.S. (2011). A gustotopic map of taste qualities in the mammalian brain. Science *333*, 1262–1266.

Chieng, B.C., Christie, M.J., and Osborne, P.B. (2006). Characterization of neurons in the rat central nucleus of the amygdala: cellular physiology, morphology, and opioid sensitivity. J. Comp. Neurol. *497*, 910–927.

Ciocchi, S., Herry, C., Grenier, F., Wolff, S.B., Letzkus, J.J., Vlachos, I., Ehrlich, I., Sprengel, R., Deisseroth, K., Stadler, M.B., et al. (2010). Encoding of conditioned fear in central amygdala inhibitory circuits. Nature *468*, 277–282.

Craig, A.D. (2003). Interoception: the sense of the physiological condition of the body. Curr. Opin. Neurobiol. *13*, 500–505.

Curtu, R., Shpiro, A., Rubin, N., and Rinzel, J. (2008). Mechanisms for frequency control in neuronal competition models. Siam J. Appl. Dyn. Syst. *7*, 609–649.

Day, H.E., Curran, E.J., Watson, S.J., Jr., and Akil, H. (1999). Distinct neurochemical populations in the rat central nucleus of the amygdala and bed nucleus of the stria terminalis: evidence for their selective activation by interleukin-1beta. J. Comp. Neurol. *413*, 113–128.

Destexhe, A., and Sejnowski, T.J. (2009). The Wilson-Cowan model, 36 years later. Biol. Cybern. *101*, 1–2.

Douglass, A.M., Kucukdereli, H., Ponserre, M., Markovic, M., Grundemann, J., Strobel, C., Alcala Morales, P.L., Conzelmann, K.K., Luthi, A., and Klein, R. (2017). Central amygdala circuits modulate food consumption through a positive-valence mechanism. Nat. Neurosci. *20*, 1384–1394.

Dumont, E.C., Martina, M., Samson, R.D., Drolet, G., and Pare, D. (2002). Physiological properties of central amygdala neurons: species differences. Eur. J. Neurosci. *15*, 545–552.

Duvarci, S., Popa, D., and Pare, D. (2011). Central amygdala activity during fear conditioning. J. Neurosci. *31*, 289–294.

Fadok, J.P., Markovic, M., Tovote, P., and Luthi, A. (2018). New perspectives on central amygdala function. Curr. Opin. Neurobiol. *49*, 141–147.

Fudge, J.L., and Tucker, T. (2009). Amygdala projections to central amygdaloid nucleus subdivisions and transition zones in the primate. Neuroscience *159*, 819–841.

Gehrlach, D.A., Dolensek, N., Klein, A.S., Roy Chowdhury, R., Matthys, A., Junghanel, M., Gaitanos, T.N., Podgornik, A., Black, T.D., Reddy Vaka, N., et al. (2019). Aversive state processing in the posterior insular cortex. Nat. Neurosci. *22*, 1424–1437.

Gilpin, N.W., Herman, M.A., and Roberto, M. (2015). The central amygdala as an integrative hub for anxiety and alcohol use disorders. Biol. Psychiatry *77*, 859–869.

Gogolla, N. (2017). The insular cortex. Curr. Biol. *27*, R580–R586.

Hardaway, J.A., Halladay, L.R., Mazzone, C.M., Pati, D., Bloodgood, D.W., Kim, M., Jensen, J., DiBerto, J.F., Boyt, K.M., Shiddapur, A., et al. (2019). Central amygdala prepronociceptin-expressing neurons mediate palatable food consumption and reward. Neuron *102*, 1037–1052.e7.

Haubensak, W., Kunwar, P.S., Cai, H., Ciocchi, S., Wall, N.R., Ponnusamy, R., Biag, J., Dong, H.W., Deisseroth, K., Callaway, E.M., et al. (2010). Genetic dissection of an amygdala microcircuit that gates conditioned fear. Nature *468*, 270–276.

Hou, W.H., Kuo, N., Fang, G.W., Huang, H.S., Wu, K.P., Zimmer, A., Cheng, J.K., and Lien, C.C. (2016). Wiring specificity and synaptic diversity in the mouse lateral central amygdala. J. Neurosci. *36*, 4549–4563.

Hunt, S., Sun, Y., Kucukdereli, H., Klein, R., and Sah, P. (2017). Intrinsic circuits in the lateral central amygdala. eNeuro *4*, e0367–16.2017.

Ip, C.K., Zhang, L., Farzi, A., Qi, Y., Clarke, I., Reed, F., Shi, Y.C., Enriquez, R., Dayas, C., Graham, B., et al. (2019). Amygdala NPY circuits promote the development of accelerated obesity under chronic stress conditions. Cell Metab. *30*, 111–128.e6.

Isosaka, T., Matsuo, T., Yamaguchi, T., Funabiki, K., Nakanishi, S., Kobayakawa, R., and Kobayakawa, K. (2015). Htr2a-expressing cells in the central amygdala control the hierarchy between innate and learned fear. Cell *163*, 1153–1164.

Izhikevich, E. (2007). Dynamical Systems in Neuroscience (MIT Press).

Janak, P.H., and Tye, K.M. (2015). From circuits to behaviour in the amygdala. Nature *517*, 284–292.

Johansen, J.P., Cain, C.K., Ostroff, L.E., and Ledoux, J.E. (2011). Molecular mechanisms of fear learning and memory. Cell *147*, 509–524.

Katz, D.B., Simon, S.A., and Nicolelis, M.A. (2001). Dynamic and multimodal responses of gustatory cortical neurons in awake rats. J. Neurosci. *21*, 4478–4489.

Kim, J., Zhang, X., Muralidhar, S., LeBlanc, S.A., and Tonegawa, S. (2017). Basolateral to central amygdala neural circuits for appetitive behaviors. Neuron *93*, 1464–1479.e5.

LeDoux, J.E. (2000). Emotion circuits in the brain. Annu. Rev. Neurosci. *23*, 155–184.

Li, H., Penzo, M.A., Taniguchi, H., Kopec, C.D., Huang, Z.J., and Li, B. (2013). Experience-dependent modification of a central amygdala fear circuit. Nat. Neurosci. *16*, 332–339.

Lopez de Armentia, M., and Sah, P. (2004). Firing properties and connectivity of neurons in the rat lateral central nucleus of the amygdala. J. Neurophysiol. *92*, 1285–1294.

Madisen, L., Zwingman, T.A., Sunkin, S.M., Oh, S.W., Zariwala, H.A., Gu, H., Ng, L.L., Palmiter, R.D., Hawrylycz, M.J., Jones, A.R., et al. (2010). A robust and high-throughput Cre reporting and characterization system for the whole mouse brain. Nat. Neurosci. *13*, 133–140.

McDonald, A.J., and Augustine, J.R. (1993). Localization of GABA-like immunoreactivity in the monkey amygdala. Neuroscience *52*, 281–294.

McDonald, A.J., Shammah-Lagnado, S.J., Shi, C., and Davis, M. (1999). Cortical afferents to the extended amygdala. Ann. N. Y Acad. Sci. *877*, 309–338.

Mufson, E.J., Mesulam, M.M., and Pandya, D.N. (1981). Insular interconnections with the amygdala in the rhesus monkey. Neuroscience *6*, 1231–1248.

Palmiter, R.D. (2018). The parabrachial nucleus: CGRP neurons function as a general alarm. Trends Neurosci. *41*, 280–293.

Petrovich, G.D., Ross, C.A., Mody, P., Holland, P.C., and Gallagher, M. (2009). Central, but not basolateral, amygdala is critical for control of feeding by aversive learned cues. J. Neurosci. *29*, 15205–15212.

Rangan, A.V., and Young, L.S. (2013). Emergent dynamics in a model of visual cortex. J. Comput. Neurosci. *35*, 155–167.

Ressler, R.L., and Maren, S. (2019). Synaptic encoding of fear memories in the amygdala. Curr. Opin. Neurobiol. *54*, 54–59.

Rich, S., Booth, V., and Zochowski, M. (2016). Intrinsic cellular properties and connectivity density determine variable clustering patterns in randomly connected inhibitory neural networks. Front. Neural Circ. *10*, 82.

Rowat, P.F., and Selverston, A.I. (1997). Oscillatory mechanisms in pairs of neurons connected with fast inhibitory synapses. J. Comput. Neurosci. *4*, 103–127.

Rush, M.E., and Rinzel, J. (1995). The potassium A-current, low firing rates and rebound excitation in Hodgkin-Huxley models. Bull. Math. Biol. *57*, 899–929.

Sah, P., Faber, E.S., Lopez De Armentia, M., and Power, J. (2003). The amygdaloid complex: anatomy and physiology. Physiol. Rev. *83*, 803–834.

Samuelsen, C.L., and Fontanini, A. (2017). Processing of intraoral olfactory and gustatory signals in the gustatory cortex of awake rats. J. Neurosci. *37*, 244–257.

Schiff, H.C., Bouhuis, A.L., Yu, K., Penzo, M.A., Li, H., He, M., and Li, B. (2018). An insula-central amygdala circuit for guiding tastant-reinforced choice behavior. J. Neurosci. *38*, 1418–1429.

Selverston, A. (2008). Stomatogastric ganglion. Scholarpedia *3*, 1661.

Shi, C.J., and Cassell, M.D. (1998). Cortical, thalamic, and amygdaloid connections of the anterior and posterior insular cortices. J. Comp. Neurol. *399*, 440–468.

Shpiro, A., Curtu, R., Rinzel, J., and Rubin, N. (2007). Dynamical characteristics common to neuronal competition models. J. Neurophysiol. *97*, 462–473.

Skinner, F.K., and Mulloney, B. (1998). Intersegmental coordination of limb movements during locomotion: mathematical models predict circuits that drive swimmeret beating. J. Neurosci. *18*, 3831–3842.

Stern, S.A., Pomeranz, L.E., Azevedo, E.P., Doerig, K.R., and Friedman, J.M. (2019). A molecularly defined insular cortex–> central amygdala circuit mediates conditioned overconsumption of food. BioRxiv. https://doi.org/10.1101/684498.

Sun, N., and Cassell, M.D. (1993). Intrinsic GABAergic neurons in the rat central extended amygdala. J. Comp. Neurol. *330*, 381–404.

Terman, D., Rubin, J.E., Yew, A.C., and Wilson, C.J. (2002). Activity patterns in a model for the subthalamopallidal network of the basal ganglia. J. Neurosci. *22*, 2963–2976.

Tervo, D.G., Hwang, B.Y., Viswanathan, S., Gaj, T., Lavzin, M., Ritola, K.D., Lindo, S., Michael, S., Kuleshova, E., Ojala, D., et al. (2016). A designer AAV variant permits efficient retrograde access to projection neurons. Neuron *92*, 372–382.

Thompson, J.M., and Neugebauer, V. (2017). Amygdala plasticity and pain. Pain Res. Manag. *2017*, 8296501.

van den Burg, E.H., and Stoop, R. (2019). Neuropeptide signalling in the central nucleus of the amygdala. Cell Tissue Res. *375*, 93–101.

Wang, L., Gillis-Smith, S., Peng, Y., Zhang, J., Chen, X., Salzman, C.D., Ryba, N.J.P., and Zuker, C.S. (2018). The coding of valence and identity in the mammalian taste system. Nature *558*, 127–131.

Werner, B., and Spence, A. (1984). The computation of symmetry-breaking bifurcation points. Siam J. Numer. Anal. *21*, 388–399.

Wilson, H.R., and Cowan, J.D. (1973). A mathematical theory of the functional dynamics of cortical and thalamic nervous tissue. Kybernetik *13*, 55–80.

Wilson, T.D., Valdivia, S., Khan, A., Ahn, H.S., Adke, A.P., Martinez Gonzalez, S., Sugimura, Y.K., and Carrasquillo, Y. (2019). Dual and opposing functions of the central amygdala in the modulation of pain. Cell Rep. *29*, 332–346.e5.

Yamamoto, T., Yuyama, N., Kato, T., and Kawamura, Y. (1985). Gustatory responses of cortical neurons in rats. II. Information processing of taste quality. J. Neurophysiol. *53*, 1356–1369.

Zhang, C., Guy, R.D., Mulloney, B., Zhang, Q., and Lewis, T.J. (2014). Neural mechanism of optimal limb coordination in crustacean swimming. Proc. Natl. Acad. Sci. U S A *111*, 13840–13845.

Zhang, F., Aravanis, A.M., Adamantidis, A., de Lecea, L., and Deisseroth, K. (2007). Circuit-breakers: optical technologies for probing neural signals and systems. Nat. Rev. Neurosci. *8*, 577–581.

iScience, Volume *23*

Supplemental Information

Neural Circuit Mechanism Underlying the Feeding Controlled by Insula-Central Amygdala Pathway

Calvin Zhang-Molina, Matthew B. Schmit, and Haijiang Cai

Neural circuit mechanism underlying the feeding controlled by insula-central amygdala pathway

Calvin Zhang-Molina[a,1], Matthew B Schmit[b,c] & Haijiang Cai[b,d,1]

a. Department of Mathematics, University of Arizona, Tucson, AZ 85721 USA.
b. Department of Neuroscience, University of Arizona, Tucson, AZ, 85721, USA.
c. Graduate Interdisciplinary Program in Neuroscience, University of Arizona, Tucson, AZ, 85721, USA.
d. Bio5 Institute and Department of Neurology, University of Arizona, Tucson, AZ, 85721, USA.
1. To whom correspondence may be addressed. Email: calvinz@math.arizona.edu or haijiangcai@email.arizona.edu

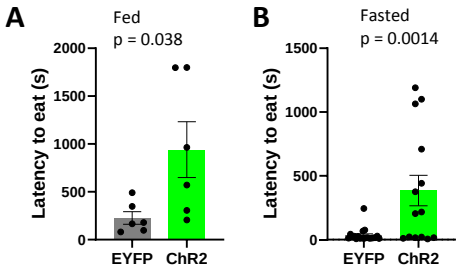

Figure S1, related to Figure 1. Initiation of feeding was suppressed in both fed (A) and fasted states (B). Light activation of the insula-CeA projections increases the latency to eat. The latency was defined from the presence of the food pellet to the first bite. Unpaired *t*-test, fed state, $t_{(10)} = 2.39$. n = 6 animals in each group; $t_{(32)} = 3.50$. n = 20 animals expressing EYFP and 14 animals expressing ChR2.

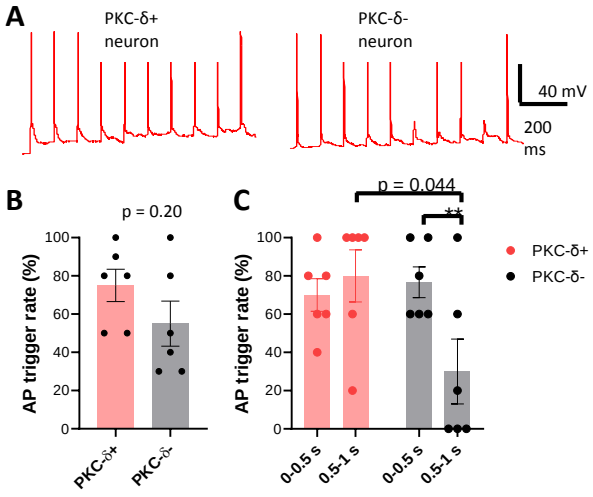

Figure S2, related to Figure 4. Action potentials (AP) in CeA neurons triggered by 10 Hz light stimulation of the insular terminals in CeA. **A**. Representative brain slice electrophysiological recordings show AP in PKC-δ+ and PKC-δ- neurons. **B**. The overall AP trigger rate is not different between PKC-δ+ and PKC-δ- neurons. Unpaired *t*-test, $t_{(10)} = 1.38$. n = 6 cells in each group. **C**. PKC-δ- neurons show a decreased AP trigger rate (adaption) while PKC-δ+ neurons does not. For PKC-δ- neurons, paired *t*-test, $t_{(5)} = 4.18$ ** $p < 0.01$, n = 6 cells in each group. Comparison at 0.5-1 s between PKC-δ+ and PKC-δ- neurons, unpaired *t*-test, $t_{(10)} = 2.30$. n = 6 cells in each group.

Transparent Methods

Key resources table

REAGENT	SOURCE	IDENTIFIER
Virus		
AAV2-EF1a-DIO-hChR2(H134R)-EYFP-WPRE-pA	UNC, Deisseroth	
AAV2-EF1a-DIO-EYFP-WPRE-pA	UNC, Deisseroth	
AAV2-CMV-Cre-WPRE-SV40	UNC, Deisseroth	
AAV2-hSyn-ChR2-EYFP	UNC, Deisseroth	
rAAV2-Retro/CAG-Cre	UNC, Boyden	
Organisms/Strains		Stock #
Wild-type mice (C57BL/6)	Charles River Laboratories	C57BL/6
PKC-δ-ires-Cre line	Caltech, David Anderson lab	
Ai 14 Cre reporter mice	Jackson Lab	007914

Contact for reagent and resource sharing

Requests for further information or biological resources and reagents should be directed to and will be fulfilled by Haijiang Cai (haijiangcai@email.arizona.edu). Request for mathematical modeling and Matlab coding should be directed to and will be fulfilled by Calvin Zhang-Molina (calvinz@math.arizona.edu).

Mice

All mice used in this project are offspring from PKC-δ-Cre mice crossed with wild type C57BL/6crl mice from the Charles River Laboratory (a background used in our previous study (Cai et al., 2014)) for at least 5 to 6 generations. The genotype of offspring was identified by PCR on genomic tail DNA. Only male wild type and PKC-δ-Cre offspring were used in this study. All mice were housed on a 12-hour light (7 am)/dark (7 pm) cycle with *ad libitum* access to water and rodent chow unless placed on a food restriction schedule for fasted feeding experiments. All behavioral experiments and brain slice electrophysiology were performed during the light cycle. All animal care and experimental procedures were strictly conducted according to the guidelines of US National Institutes of Health for animal research and were approved by the Institutional Animal Care and Use Committee (IACUC) at the University of Arizona.

Virus

All the viruses used in this study were purchased from the University of North Carolina Viral Vector Core. AAV2retro-Cre vector was originally generated in Dr. Ed Boyden's lab at M.I.T. AAV2-EF1a-DIO-EYFP-WPRE-pA, AAV2-EF1a-DIO-hChR2(H134R)-EYFP-WPRE-pA, AAV2-hSyn-ChR2-EYFP, AAV2-CMV-Cre-WPRE-SV40 vectors were generated in Dr. Karl Deisseroth's lab at Stanford University. All the AAV and AAV2retro viruses had titres of 1-6x10^{12} genome copies per ml. Construct validity and correct targeting to the brain nucleus of interest were confirmed through post-mortem processing of brain sections in multiple sets of mice or electrophysiological recordings on live brain slices. To minimize variation of environmental differences and virus expression level, the control virus and experimental virus were injected in the same time window by the same investigator.

Stereotaxic mice surgery

Mice at 2-3 months old were deeply anaesthetized with 5% isoflurane in oxygen and kept at 1-1.5% isoflurane throughout the surgery. Survival surgery was then performed on a stereotaxic frame (Model 1900, Kopf Instruments). An incision was made on the midline of the scalp and a craniotomy was performed above the target regions. Viruses were microinfused through a pulled-glass micropipette with 20-50 µm tip outer diameter connected with a Nanoliter Injector (Nanoliter 2010, World Precision

Instruments) at a rate of 8-10 nl/min. After injection, the micropipette was raised by 50 µm and left in place for 3-5 min to allow for diffusion of the virus liquid before the pipette was slowly withdrawn. Injection volumes into the IC and CeA were 40 nl. Viruses were injected bilaterally for behavioral studies and unilaterally for slice electrophysiology. Injection coordinates (in mm) relative to midline and Bregma: insular cortex (±3.90, 0, -3.83), CeA (±2.85, -1.40, -4.73). Optical ferrule fibers were implanted bilaterally ~0.5 mm above the injection coordinates. After ferrule fiber implantation, dental cement (C&B Metabond) was used to secure the fiber to the skull. For postoperative care, mice were injected intraperitoneally with ketoprofen (5 mg/kg) daily for 3 days. At least 3 weeks after surgery were allowed for recovery and viral expression before the behavioral assays.

***In vivo* Optogenetics**

A blue (Shanghai DreamLaser: 473 nm, 100 mW or 50 mW) or yellow (Shanghai DreamLaser: 593 nm, 100 mW) laser was used to deliver light stimulation. An Accupulser Signal Generator (World Precision Instruments, SYS-A310) was used to control the frequency and pulse width of the laser light. Light was delivered to the brain through an optic fiber (200 µm diameter, NA 0.22, Doric Lenses) connected with the implanted ferrule fiber by a zirconium sleeve. The light power in the brain regions 0.5 mm below the fiber tip was calibrated (Aravanis et al., 2007). The calibrated light power density (0.5 mm below the fiber tip) used in light activation experiment was ~5 mW/mm^2. 10 Hz, 10-ms (pulse width) light pulse trains were used in optogenetic activation experiments.

Feeding assays

Mice were transferred into an empty testing cage in the behavioral testing room to habituate for at least 20 min one day before the feeding test. For the 24-hr fasted feeding test, mice were food-deprived while have access to water. Mice were briefly anaesthetized with isoflurane (< 1 min) and coupled with optic fibers before the experiments. At least 20 min after recovery in behavioral testing room, mice were introduced into a clean empty testing cage with a pre-weighed regular food pellet, and allowed to feed for 20 min. The body weight of the mice before test, weight of food pellet before and after test, including the food debris left in the cage floor after test, were measured to calculate the amount of food intake. For the feeding test at fed state, mice were not food deprived before testing, and allowed to feed for 30 min. For optogenetic experiments, the light was delivered just after the mice were introduced into the testing cage. After each test, mice were returned to their home cage with *ad libitum* access to water and rodent chow. For the home cage feeding test, mice were food deprived for 24 hours. A single food pellet was placed in the home cage at the beginning of the test and the animal was allowed to eat for 10 min. Activation light (473 nm) was triggered 1-2 seconds after each feeding behavior began. 10 Hz, 10-ms light pulses were delivered until 1-5 seconds after the cessation of each feeding. The feeding behavior was videotaped and manually analyzed with a MATLAB based in-house behavioral annotation script.

Open field test

A white square box (50 × 50 × 30 cm, a 25 × 25 cm square center was defined as “center” in analysis) was used as open field box. Mice were placed individually in the center of the box, and their behavior was tracked for 6 min in optogenetic tests with 2 minutes of light stimulation (473 nm, 10 ms pulse, 10 Hz) applied 2 minutes after the start. All the behaviors were videotaped and analyzed offline with Ethovision.

Histology

All mice after behavioral tests were deeply anesthetized with ketamine/xylazine (100/20 mg/ml). Mice were then transcardially perfused with 20-ml PBS followed by 20-ml of 4% paraformaldehyde in PBS. Brains were removed and post-fixed in 4% paraformaldehyde overnight before being rinsed twice with PBS. The brains were sectioned with a vibratome (Leica, VT1000S) at 50-100 µm thickness and plated for

imaging. The expression of virus and position of implanted optic fibers were checked with a fluorescence microscope.

Electrophysiological slice recordings

Brain coronal sections were sectioned at 250 μm thickness with a Leica vibratome (VT1000S) in ice cold glycerol-based artificial cerebrospinal fluid (GACSF) containing 252 mM glycerol, 1.6 mM KCl, 1.2 mM NaH_2PO_4, 1.2 mM $MgCl_2$, 2.4 mM $CaCl_2$, 18 mM $NaHCO_3$, 11 mM glucose, oxygenated with carbogen (95% O_2 balanced with CO_2 for at least 15 min before use. The brain sections after cutting were recovered for at least one hour at 32-34 °C in regular ACSF containing 126 mM NaCl, 1.6 mM KCl, 1.2 mM NaH_2PO_4, 1.2 mM $MgCl_2$, 2.4 mM $CaCl_2$, 18 mM $NaHCO_3$, 11 mM glucose, oxygenated with carbogen. The recordings were performed in a rig equipped with a fluorescence microscope (Olympus BX51), MultiClamp 700B and Digidata 1550A1 (Molecular Devices). The patch pipettes with a resistance of 5-10 MΩ were pulled with P-97 Sutter micropipetter puller and filled with an intracellular solution (135 mM potassium gluconate, 5 mM EGTA, 0.5 mM $CaCl_2$, 2 mM $MgCl_2$, 10 mM HEPES, 2 mM MgATP and 0.1 mM GTP, pH 7.3-7.4, 290–300 mOsm). Recording data were sampled at 10 kHz, filtered at 3 kHz and analyzed with pCLAMP10. tdTomato expression were usually verified post recording using a RFP filter. For the optogenetic stimulation, a blue laser (Shanghai DreamLaser, 473 nm, 50 mW) was used to deliver light pulses (0.1-2 mW/mm^2 at the tip). 2 ms light pulses were used to activate the nerve terminals from insular cortex to trigger action potentials or induce postsynaptic responses in CeA neurons. EPSCs were measured when cells were voltage-clampped at -70 mV, a 0.1 μs 0.1 mV was applied at the same time of light delivery to help identify the start of light pulse. The action potentials were triggered when cells were current-clampped at -65 mV.

Quantification and statistical analysis

Unless indicated, Data represent mean ± s.e.m. Unpaired Student's *t*-test or Mann-Whitney rank test was used to compare two groups. A *p* value smaller than 0.05 was considered significant. Data were analyzed with GraphPad Prism Software, R and RStudio (538.1 Qt/5.4.1).

Mathematical model

In this subsection, we introduce and describe our mathematical model of the CeA circuit. We first describe the mathematical equations for each model neuron in the CeA circuit. In our model, the state of each model neuron is completely described by its membrane potential and the gating variables of its intrinsic and synaptic ionic currents, whose activities are altogether governed by a set of Hodgkin-Huxley-type equations that produce a prescribed electrophysiological property of either regular spiking or late firing. Here, the phrase "late firing" refers to a relatively long *onset firing wait time*, which measures the elapsed time from when a depolarization current step is injected to the cell to when the cell fires an action potential (if the depolarization current was sufficient to trigger the firing event). Experimental results have shown that onset delay recordings from central amygdala neurons fall into two clusters: one with short delays (or almost no delay), and the other with long delays (Chieng et al., 2006; Dumont et al., 2002; Lopez de Armentia and Sah, 2004). Those central amygdala neurons that exhibit short or no delay in onset firing are called regular spiking CeA neurons, and those with a long onset delay are called late firing CeA neurons.

For each of the regular spiking CeA model neurons, we use the standard Hodgkin-Huxley equations (Ermentrout and Terman, 2010):

$$C\frac{dV_i}{dt} = \bar{g}_{\mathrm{K}} n_i^4 (E_{\mathrm{K}} - V_i) + \bar{g}_{\mathrm{Na}} m_i^3 h_i (E_{\mathrm{Na}} - V_i) + g_{\mathrm{L}} (E_{\mathrm{L}} - V_i) + I_{\mathrm{bias}} + I_i^{\mathrm{ext}} + \sum_j I_{ij}^{\mathrm{syn}},$$

$$\frac{dx_i}{dt} = \alpha_x(V_i)(1 - x_i) + \beta_x(V_i)x_i, \qquad (x = n, m, \text{and } h)$$

in which V_i is the membrane potential of model neuron *i* (*i* can be LF1, LF2, RS, LF, RS1, or RS2), n_i is the activation gating variable of the K^+ current, m_i is the activation gating variable of the Na^+ current, h_i is the inactivation gating variable of the Na^+ current, $\bar{g}_{\mathrm{K}}$ is the maximum conductance of the K^+ current, $\bar{g}_{\mathrm{Na}}$ is the maximum conductance of the Na^+ current, g_{L} is the conductance of the leakage current, $\sum_j I_{ij}^{\mathrm{syn}}$ is the sum of all postsynaptic currents in neuron *i* due to activity in neuron *j* (*j* can be LF2, LF1, RS, LF, RS2, or RS1; this synaptic current will be defined later), E_{K}, E_{Na} and E_{L} are the reversal potentials of the K^+, Na^+, and leakage currents, respectively, I_{bias} is the bias current, I_i^{ext} is the external current injection representing the activation input from the insular cortex to each neuron, *C* is the membrane capacitance, and the voltage-dependent gating functions are

$$\alpha_n(V) = \frac{0.00025(V + 55)}{1 - \exp\left(-\frac{V + 55}{10}\right)},$$

$$\beta_n(V) = 0.003125 \exp\left(-\frac{V + 65}{80}\right),$$

$$\alpha_m(V) = \frac{0.1(V + 40)}{1 - \exp\left(-\frac{V + 40}{10}\right)},$$

$$\beta_m(V) = 4 \exp\left(-\frac{V + 65}{18}\right),$$

$$\alpha_h(V) = 0.07 \exp\left(-\frac{V + 65}{20}\right),$$

$$\beta_h(V) = \frac{1}{1 + \exp\left(-\frac{V + 35}{10}\right)}.$$

See figure captions for parameter values used in the computer simulations. Note that we use the same parameters for all computer simulations unless otherwise stated when performing a bifurcation analysis.

For each of the late firing CeA model neurons, we modify the standard Hodgkin-Huxley equations by including a potassium A-type current to the membrane potential equation (see the first term on the right-hand-side of the equation):

$$C\frac{dV_i}{dt} = \bar{g}_{\mathrm{A}}A_\infty(V_i)^3B(E_{\mathrm{K}} - V_i) + \bar{g}_{\mathrm{K}}n_i^4(E_{\mathrm{K}} - V_i) + \bar{g}_{\mathrm{Na}}m_i^3h_i(E_{\mathrm{Na}} - V_i) + g_{\mathrm{L}}(E_{\mathrm{L}} - V_i) + I_{\mathrm{bias}} + I_i^{\mathrm{ext}} + \sum_j I_{ij}^{\mathrm{syn}},$$

where the time evolution of the inactivation gating variable *B* of this A-type K^+ current is governed by

$$\frac{dB}{dt} = \frac{1}{\tau_B}(B_\infty(V_i) - B),$$

in which τ_B is the time constant for the inactivation of this A-type current, and the activation and inactivation gating functions are given by, respectively,

$$A_\infty(V) = \frac{1}{1 + \exp\left(-\frac{V + 78}{50}\right)},$$

$$B_\infty(V) = \frac{1}{1 + \exp\left(\frac{V + 73}{6}\right)},$$

and all the other ionic currents are governed by the same equations as defined earlier in the case of a regular spiking neuron. Note that the inclusion of this fast-activation and slow-inactivation outward A-type current gives rise to a dynamical mechanism that produces delayed onset firing (Rush and Rinzel, 1995); by adjusting the time constant τ_B of the slow current inactivation, we can achieve a good range of spike onset delay (see Fig. 7).

Finally, we describe the mathematical equations for the synaptic connections among the CeA model neurons. We use a conductance-based synaptic current model for each inhibitory synaptic connection in which the gating variable itself is a dynamic variable following first-order kinetics (recall that experimental evidence suggests the lack of excitatory connections among the different CeA neural populations):

$$I_{ij}^{\text{syn}} = \bar{g}_{ij}^{\text{syn}} s_{ij}\left(E_{\text{syn}} - V_i\right),$$
$$\frac{ds_{ij}}{dt} = \alpha_s\left(V_j\right)\left(1 - s_{ij}\right) + \beta_s\left(V_j\right)s_{ij}.$$

Recall that I_{ij}^{syn} is the postsynaptic conductance in neuron *i* due to activity in neuron *j*, in which s_{ij}, $\bar{g}_{ij}^{\text{syn}}$ and E_{syn} are the gating variable, maximum conductance and reversal potential of this synaptic current, respectively, and the voltage-dependent gating functions are

$$\alpha_s(V) = \frac{0.025}{1 + \exp\left(-\frac{V + 28}{10}\right)},$$
$$\beta_s(V) = 0.025 - \frac{0.025}{1 + \exp\left(-\frac{V + 28}{10}\right)}.$$

Supplementary References

Aravanis, A.M., Wang, L.P., Zhang, F., Meltzer, L.A., Mogri, M.Z., Schneider, M.B., and Deisseroth, K. (2007). An optical neural interface: in vivo control of rodent motor cortex with integrated fiberoptic and optogenetic technology. Journal of neural engineering *4*, S143-156.

Cai, H., Haubensak, W., Anthony, T.E., and Anderson, D.J. (2014). Central amygdala PKC-delta(+) neurons mediate the influence of multiple anorexigenic signals. Nat Neurosci *17*, 1240-1248.

Chieng, B.C., Christie, M.J., and Osborne, P.B. (2006). Characterization of neurons in the rat central nucleus of the amygdala: cellular physiology, morphology, and opioid sensitivity. J Comp Neurol *497*, 910-927.

Dumont, E.C., Martina, M., Samson, R.D., Drolet, G., and Pare, D. (2002). Physiological properties of central amygdala neurons: species differences. Eur J Neurosci *15*, 545-552.

Ermentrout, G., and Terman, D. (2010). The Hodgkin-Huxley Equations. Mathematical Foundations of Neuroscience pp 1-28, Springer, New York, NY.

Lopez de Armentia, M., and Sah, P. (2004). Firing properties and connectivity of neurons in the rat lateral central nucleus of the amygdala. J Neurophysiol *92*, 1285-1294.

Rush, M.E., and Rinzel, J. (1995). The potassium A-current, low firing rates and rebound excitation in Hodgkin-Huxley models. Bull Math Biol *57*, 899-929.